Title: Neural signatures of auditory hypersensitivity following acoustic trauma

Authors: Matthew McGill[1-2+], Ariel E. Hight[1-2*], Yurika L. Watanabe[1], Aravindakshan Parthasarathy[1,3^], Dongqin Cai[1,3], Kameron Clayton[1,3], Ken Hancock[1,3], Anne Takesian[1,3], Sharon G. Kujawa[1,3], and Daniel B. Polley[1,3]

1- Eaton-Peabody Laboratories, Massachusetts Eye and Ear Infirmary, Boston MA 02114 USA
2- Division of Medical Sciences, Harvard Medical School, Boston MA 02114
3- Dept. Otolaryngology - Head and Neck Surgery, Harvard Medical School, Boston MA 02114 USA

* Present address: Department of Otolaryngology-Head and Neck Surgery, New York University School of Medicine, New York, New York 10016 USA
^ Present address: Department of Communication Science and Disorders, University of Pittsburgh, Pittsburgh PA 15260 USA
+ Lead contact: mmcgill@harvard.edu

Keywords: homeostatic plasticity, compensatory plasticity, two-photon calcium imaging, excess central gain, hearing loss, loudness recruitment, hyperacusis, tinnitus

ABSTRACT

Throughout the brain, neurons exhibit a remarkable capacity to maintain stable firing rates despite large perturbations in afferent activity levels. As an exception, homeostatic regulation of neural activity often fails in the adult auditory system after hearing loss. Cochlear deafferentation caused by aging or noise exposure triggers widespread neural hyperactivity, particularly in the auditory cortex (ACtx), which underlies perceptual disorders including tinnitus and hyperacusis. Here, we show that mice with noise-induced damage of the high-frequency cochlear base were behaviorally hypersensitive to spared mid-frequency tones and to direct optogenetic stimulation of auditory thalamocortical neurons. Chronic 2-photon calcium imaging from ACtx pyramidal neurons (PyrNs) revealed an initial stage of diffuse hyperactivity, hypercorrelation, and hyperresponsivity that consolidated around deafferented map regions three or more days after acoustic trauma. Deafferented PyrN ensembles displayed hypersensitive decoding of spared mid-frequency tones, mirroring behavioral hypersensitivity. At the level of individual PyrNs, some exhibited stable, homeostatic gain control after acoustic trauma, while others showed non-homeostatic excess gain. Interestingly, factors such as baseline spontaneous activity levels and sound level encoding could account for 40% of the variability in PyrN gain regulation after acoustic trauma. These findings suggest that non-homeostatic regulation of cortical sound intensity coding following sensorineural loss may underlie the well-established clinical phenomenon of loudness hypersensitivity. Further, while cortical gain changes are triggered by reduced bottom-up afferent input, their subsequent stabilization is also shaped by their local circuit milieu, where baseline response features can identify neurons with the greatest propensity for developing pathological hyperactivity following sensorineural hearing loss.

INTRODUCTION

Sensory disorder research typically focuses on the mechanisms underlying inherited or acquired forms of sensory loss. But one of the most common and debilitating sensory disorder phenotypes reflect just the opposite problem; not what cannot be perceived, but what cannot *stop* being perceived. Sensory overload typically presents as three co-morbid and inter-related features: *i) an* irrepressible perception of phantom stimuli that have no physical environmental source, *ii)* a selective inability to perceptually suppress distracting sensory features, and *iii*) the perception that moderate stimuli are uncomfortably intense, distressing, or even painful. One or more of these phenotypes are commonly observed in heterogeneous neurological and psychiatric disorders including autism spectrum disorder (Klintwall et al., 2011; Robertson and Baron-Cohen, 2017), post-traumatic stress disorder (Ehlers and Clark, 2000; Garfinkel and Liberzon, 2009), fibromyalgia (Nielsen and Henriksson, 2007; Yunus, 2007), schizophrenia (González-Rodríguez et al., 2021; Luck and Gold, 2008), traumatic brain injury (Nampiaparampil, 2008), sensorineural hearing loss (Auerbach et al., 2014; Hebert et al., 2013; Pienkowski et al., 2014a), attention deficit hyperactivity disorder (Ghanizadeh, 2011), migraine (Goadsby et al., 2017), and also as a consequence of normal aging (Herrmann and Butler, 2021a; Nusbaum, 1999).

Although overload phenotypes are reported across sensory modalities, they are most common and debilitating in hearing, where an estimated 14% of adult population continuously perceives a phantom ringing or buzzing sound (i.e., tinnitus) (Shargorodsky et al., 2010), 9% of adults report hypersensitivity to ordinary environmental sounds (i.e., hyperacusis, or loudness hypersensitivity) (Pienkowski et al., 2014a, 2014b), and 9% of adults seek health care for poor hearing in complex listening environments but do not have hearing loss (Parthasarathy et al., 2020a). Although one or more of these auditory overload phenotypes can occur without evidence of cochlear dysfunction, they are far more common in persons with sensorineural hearing loss (SNHL) arising from age- or noise-induced degeneration of cochlear hair cells and cochlear afferent nerve terminals (for review see Auerbach and Gritton, 2022; Herrmann and Butler, 2021b; Noreña, 2011; Zeng, 2013).

Phantom percepts, hypersensitivity, and poor distractor suppression are thought to arise from abnormal elevations and patterning of neural activity in central sensory pathways. In the auditory system, sensorineural damage in the cochlea reduces the volume of electrical activity reaching the brainstem from the auditory nerve. Afferent loss is registered by central auditory neurons via decreased cytosolic calcium levels, which triggers a cascade of genetic, epigenetic, post-transcriptional, and post-translational processes that collectively adjust the electrical excitability of neurons to restore activity back to the baseline set point (for review see Harris and Rubel, 2006; Turrigiano, 2012). These changes can be grouped into three categories: 1) synaptic sensitization via upregulation of receptors for excitatory neurotransmitters (e.g., AMPA receptor scaling) (Balaram et al., 2019; Kotak et al., 2005; Sturm et al., 2017; Teichert et al., 2017; Sungchil Yang et al., 2011); 2) synaptic disinhibition via removal of inhibitory neurotransmitter receptors (Balaram et al., 2019; Sanes and Kotak, 2011; Sarro et al., 2008; Sturm et al., 2017; Sungchil Yang et al., 2011); 3) increased intrinsic excitability via changes in the amount and subunit composition of

voltage-gated ion channels that set the resting membrane potential, membrane resistance, and spike "burstiness" (Li et al., 2015, 2013; Pilati et al., 2012; Wu et al., 2016; Yang et al., 2012). These changes are often described as homeostatic plasticity, but in the context of adult plasticity after hearing loss they reflect a failure in homeostatic processes that maintain neural excitability at a stable set point. Whereas homeostatic changes – by definition – restore neural activity to a baseline activity rate following a perturbation (Turrigiano, 2012), neural gain adjustments following adult-onset hearing loss often over-shoot the mark, producing catastrophic downstream consequences at the level of network excitability and sound perception (Eggermont, 2017; Noreña, 2011).

Pinpointing the connection between excess neural gain and perceptual hypersensitivity disorders requires translating molecular and synaptic changes into measurements that can be made in intact and even behaving animals. With conventional microelectrode recordings, the synaptic and intrinsic compensatory processes described above manifest as increased spontaneous activity rates, increased spike synchrony, steeper slopes of sound intensity growth functions, and poor adaptation to background noise sources (for recent review see (Auerbach and Gritton, 2022; Herrmann and Butler, 2021b). The connection between these extracellular signatures of neural gain and auditory perceptual disorders has remained obscure, in part due to a frequent reliance on involuntary behaviors with a relationship to sound perception (for review see (Boyen et al., 2015; Brozoski and Bauer, 2016; Campolo et al., 2013; Hayes et al., 2014). Further, in vivo measurements have generally taken the form of acute recordings of local field potentials or unidentified excitatory and inhibitory unit types, often in anesthetized animals, and often without detailed measurements of the peripheral insult or the topographic correspondence between neural recording sites and deafferented map regions.

Here, we developed an approach to make more direct operant behavioral measurements of acoustic and neural hypersensitivity in mice with detailed characterizations of cochlear lesions. These behavioral measurements were combined with an optical approach to visualize spontaneous and sound-evoked calcium transients in awake mice from hundreds of individual excitatory neurons spanning the entire topographic map of the primary auditory cortex (A1). By performing these measurements before and after noise-induced SNHL, we were able to return to the same neurons over a 3-4 week period to identify baseline response features that could predict whether a given neuron would subsequently exhibit stable, homeostatic activity regulation or non-homeostatic excess gain following acoustic trauma.

RESULTS

Perceptual hypersensitivity following noise-induced high-frequency sensorineural hearing loss

In humans, a steeply sloping high-frequency hearing loss is a telltale signature of SNHL (Allen and Eddins, 2010; Hannula et al., 2011). We reviewed 132,504 case records from visitors to the audiology clinic at our institution and determined that 23% of pure tone audiograms fit the description of high-frequency SNHL (**Figure 1A**), underscoring that it is a common clinical condition that is commonly related to tinnitus,

loudness hypersensitivity, and poor speech intelligibility in noise (Horwitz et al., 2002; Lewis et al., 2020; Strelcyk and Dau, 2009). To model this hearing loss profile in genetically tractable laboratory mice, we induced sensorineural hearing loss through exposure to narrow-band high frequency noise (16-32 kHz) at 103 dB SPL for 2 hours. Repeated cochlear function testing before and after noise exposure revealed a sustained elevation of high-frequency thresholds for auditory brainstem responses (ABR) and cochlear distortion product otoacoustic emissions (DPOAE) with minimal threshold elevation at low-frequencies (**Figure 1B-C**).

Post-mortem cochlear histopathology suggested an anatomical substrate for cochlear function changes due to acoustic trauma. Compared to age-matched unexposed control ears, high-frequency noise exposure eliminated approximately 50% of synaptic contacts between inner hair cells (IHCs) and primary cochlear afferent neurons in the high-frequency base of the cochlea (**Figure 1D**). Noise-induced outer hair cell (OHC) death was only observed in the high-frequency extreme of the cochlear base (**Figure 1E**), though more subtle OHC stereocilia damage was evident throughout mid- and high-frequency cochlear regions (**Figure 1F-G**).

To make a more direct comparison to clinical determination of hearing loss in humans via pure tone behavioral thresholds, we also performed behavioral tone detection in head-fixed mice (**Figure 1H**). Mice were trained to report their detection of low- or high-frequency tones (8 and 32 kHz, respectively) by licking a water reward spout shortly after tone delivery. Behavioral thresholds were determined with a modified 2-up, 1-down method-of-limits that presented a combination of liminal tone intensities along with no-tone catch trials (**Figure 1I**). Behavioral detection thresholds were measured every 1-3 days before and after noise-induced SNHL (N=7) and in control mice exposed to an innocuous noise level (sham, N=6), revealing a stable 45 dB increase in high-frequency tone threshold after traumatic noise exposure without commensurate changes in false alarm rates or low-frequency detection thresholds (**Figure 1J-K**, statistical analyses are provided in figure legends).

Behavioral hypersensitivity to cochlear lesion edge frequencies and direct auditory thalamocortical activation after SNHL.

High-frequency OHC damage was the likely source of elevated ABR (Figure 1B) DPOAE (Figure 1C) and behavioral detection (Figure 1K) thresholds. Eliminating approximately 50% of auditory nerve afferent synapses onto IHCs (Figure 1D) was not expected to affect physiological or behavioral measures of hearing threshold (Chambers et al., 2016a; Lobarinas et al., 2013) but would be expected to impact suprathreshold hearing performance. In human subjects, sensorineural hearing loss is associated with elevated audibility thresholds but a steeper growth in loudness perception at sound intensities above threshold, a phenomenon called loudness recruitment (Bacon and Oxenham, 2004). A closer inspection of the mouse psychometric detection functions for the spared low-frequency tone suggested something akin to the clinical phenomenon of loudness recruitment. Following acoustic trauma, the behavioral sensitivity index

(d-prime, or d') for 8 kHz tones grew more steeply for sound intensities near thresholds compared both to pre-exposure baseline detection functions or sham exposure controls (**Figure 2A-B**).

That intensity-detection slopes were increased for the low-frequency tone at near-threshold sound levels argues against a peripheral origin for this change and instead suggests increased gain in the central auditory pathway. To investigate this possibility more directly, we were inspired by pioneering work that directly stimulated deafferented central auditory nuclei to demonstrate a direct association between neural and behavioral hypersensitivity (Gerken, 1979). We adapted this approach using combined acoustic and optogenetic stimulation (Guo et al., 2015) to identify the involvement of auditory thalamocortical hyperactivity to perceptual hypersensitivity. We used an intersectional virus strategy to selectively activate channelrhodopsin-expressing auditory thalamocortical neurons (**Figure 2C**). Using a Go/NoGo operant task, detection probability was tested in alternating blocks for high frequency bandpass noise (centered at 32kHz) or optogenetic thalamocortical stimulation. For the first week following acoustic trauma, high-frequency detection thresholds were elevated by approximately 50 dB (N=6), whereas sham exposure had no comparable effect (N=3; **Figure 2D**). Importantly, testing in interleaved trials revealed behaviorally hypersensitivity to direct stimulation of auditory thalamocortical neurons after acoustic trauma (**Figure 2E**), demonstrating significantly increased d' across optogenetic stimulation intensities compared to sham controls (**Figure 2F**). Although acoustic trauma can introduce changes in sound processing throughout all stages of central sound processing, the observation that behavioral hypersensitivity was observed to stimulation of thalamocortical projection neurons suggests that compensatory plasticity within the ACtx would be a reasonable place to investigate the neural underpinnings of loudness hypersensitivity following acoustic trauma.

Chronic imaging in A1 reveals tonotopic remapping and dynamic spatiotemporal adjustments in neural response gain after acoustic trauma

Following topographically restricted cochlear lesions, neurons in deafferented ACtx map regions reorganize to preferentially encode spared cochlear frequencies bordering the damaged region without accompanying elevations in response threshold (Engineer et al., 2011; Norena et al., 2003; Robertson and Irvine, 1989; Seki and Eggermont, 2003a; S. Yang et al., 2011). Because the degree and form of cortical plasticity following cochlear deafferentation can differ between excitatory neurons and different types of inhibitory neurons (Masri et al., 2021; Resnik and Polley, 2021; Wang et al., 2022), we restricted ACtx activity measurements to excitatory neurons via chronic calcium imaging in *Thy1-GCaMP6s* x CBA mice, where expression of a high-sensitivity genetically encoded calcium indicator is limited to cortical PyrNs (Chen et al., 2013; Romero et al., 2019). In initial experiments, we performed widefield epifluorescence calcium imaging in awake mice, which offers simultaneous visualization of all fields within the ACtx at mesoscale resolution (**Figure 3A**). These experiments confirmed that tonotopic maps were relatively stable over ~4 weeks in mice with normal hearing experience (Issa et al., 2014; Romero et al., 2019) but

underwent large-scale reorganization throughout the week following acoustic trauma before stabilizing in a state that over-represented 8 -16 kHz tones that bordered the high-frequency cochlear lesion (**Figure 3B**).

Having confirmed that A1 was a promising target for more detailed characterizations, we changed our approach to 2-photon cellular-scale measurements of A1 layer 2/3 neurons (**Figure 3C**), a cortical layer that shows robust central gain enhancements after acoustic trauma (Parameshwarappa et al., 2022; Schormans et al., 2018). Individual L2/3 PyrNs exhibited strong tone-evoked transients and well-organized tonal receptive fields (**Figure 3D**) that were measured simultaneously across hundreds of PyrNs to reveal a coarse low-to-high frequency tonotopic gradient. We used a support vector machine (SVM) to bisect the pre-exposure A1 tonotopic map into a low-frequency intact zone and high-frequency deafferented zone (**Figure 3E, top**). By returning to the same A1 region for imaging every 1-3 days (**Figure 3F**), we confirmed that L2/3 PyrNs shifted their preferred frequency towards frequencies bordering the cochlear lesion (**Figure 3E, bottom**). Analysis of all tone-responsive PyrNs (n = 1,749 in 4 trauma mice; n = 1,748 in 4 sham mice) demonstrated that tonotopic remapping was limited to the deafferented zone (**Figure 3G**), where the percentage of L2/3 PyrNs preferentially tuned to lesion edge frequencies more than doubled following acoustic trauma (**Figure 3H**) without any systematic change in response threshold (**Figure 3I**).

A marked increase in PyrNs tuned to lesion edge frequencies could contribute to the enhanced perceptual sensitivity to 8 kHz tones identified in behavioral experiments (Figure 2). To address the potential association between the neural and perceptual changes more explicitly, we measured the growth of PyrN responses across sound intensities as a function of both where neurons were located relative to the deafferentation boundary and when – following noise exposure – the measurement was made (**Figure 4**). We first quantified neural response gain as the change in PyrN response with increasing sound intensity, where the particular range of intensities used for the calculation was determined from the overall shape of the growth function (**Figure 5A, Supp Figure 1A**).

We noted that neural gain was broadly enhanced across the tonotopic map for the first several days following trauma but then receded to only the high-frequency deafferented regions in measurements made one week or more following noise exposure (**Figure 5B**). Next, we expanded the neural gain analysis in sham and trauma mice to four stimulus frequencies: a high-frequency tone aligned to the damaged cochlear region (32 kHz), a spared low-frequency tone far from the cochlear lesion (5.7 kHz), and two spared mid-frequency tones near the edge of the cochlear lesion (8 and 11.3 kHz). Neural gain at each of the four test frequencies were measured separately for intact and deafferented cortical zones and expressed in units of fold change relative to baseline gain measured from the corresponding population response prior to noise exposure. This analysis identified several clear results: *i)* a strong initial uptick in neural gain measured in both topographic regions following trauma; *ii*) persistent (lasting greater than 1 week) increases in neural gain were observed only for spared mid-frequency tones in deafferented cortical regions; *iii)* no significant changes in neural gain were observed in sham-exposed mice (**Figure 5C**). Thus, excess central gain depends on initial sound exposure level, *where* within the cortical frequency map the cell is located, *when*

relative to exposure the measurement is made, and the proximity of the stimulus test frequency to the cochlear lesion.

Cortical hyperresponsivity and increased gain mirrors behavioral hypersensitivity to spared low-frequency inputs

In the Go/NoGo tone detection behavior, mice exhibited steepened 8 kHz detection functions after trauma (Figure 2B). Excess gain in A1 L2/3 PyrNs mirrored this result in that steepened neural growth functions were observed for 8 kHz tones over the same timescale. To more directly relate ACtx hyperactivity to perceptual hypersensitivity, we used a decoder to categorize the presence or absence of sound based on single-trial responses from hundreds of simultaneously recorded neurons located either in the intact or deafferented zone of the A1 map. This was accomplished by training an SVM classifier on PCA-decomposed population activity during short periods of tone presentation or silence (**Figure 5D**). Classification of single trial A1 ensemble responses supported the hypothesis that cortical discrimination of sound versus silence would be enhanced for low- and mid-intensity 8 kHz tones but reduced for 32 kHz tones after trauma (**Figure 5E**). Enhanced neural detection of 8 kHz tones was largely driven by PyrNs in deafferented map regions, whereas the loss of cortical sensitivity to high-frequency tones was observed in both topographic zones (**Figure 5F**).

Tracking changes in activity and local synchrony in individual PyrNs over several weeks

A principal advantage of chronic 2-photon calcium imaging lies in the ability to perform longitudinal assessment of activity changes in individual cells over relatively long time periods, essentially enabling individual cells to serve as their own control when evaluating changes after noise exposure. To track individual PyrNs over a several week period, imaging fields were first registered to a pre-exposure imaging session, and cell tracking was performed using probabilistic modeling (Sheintuch et al., 2017) (**Figure 6A-B, see Methods**). Some PyrNs could be tracked throughout all 15 imaging sessions and others just for a single session, where the overall tracking success did not vary systematically between exposure conditions (**Figure 6 – figure supplement 1A**) but did predictably vary depending on how liberal or conservative the threshold was set for chronic tracking confidence (**Figure 6 – figure supplement 1B**). Interestingly, we noted a turnover in the location of chronically tracked PyrNs exhibiting clear calcium transients related to noise exposure. Following traumatic – but not sham – noise exposure, active PyrNs appeared throughout the tonotopic map but disappeared in the high-frequency deafferented zone (**Figure 6 – figure supplement 1C**). We set criteria for identifying chronically tracked cells by creating a control scenario in which a single imaging field from eight different mice were concatenated, allowing us to quantify the occurrence of falsely identified tracked cells across sessions. We observed a clear separation in the occurrence of veridically and falsely identified cells across sessions, where falsely tracked PyrNs over eight or more sessions with a confidence threshold of 0.8 were never observed, prompting us to use these criteria for the remainder of our analyses.

Chronic cell tracking allowed us to revisit analyses of central gain at the level of individual PyrNs, rather than across PyrN populations in intact or deafferented map regions. At this higher level of spatial specificity, we noted PyrNs exhibiting no increase or a temporary increase in response to an 8 kHz tone from cells in the intact (low frequency) zone and a permanent increase in responsiveness from cells in the deafferented (high frequency) zone (**Figure 6C**). More specifically, we noted transient hyper-responsiveness from 20 to 80 dB SPL for all neurons across A1 (**Figure 6D**) followed by a second stage of 8 kHz hyper-responsivity restricted to intensities above 50 dB SPL (**Figure 6D**). These observations can account for performance changes in the population-level decoder (Figure 5E) and more generally confirm that the temporal and spatial patterns noted across populations of PyrNs are supported by commensurate plasticity of single PyrN responses.

Prior studies have noted increased spontaneous activity in acute single unit or multiunit recordings in the days following acoustic trauma, though it has not been clear whether that is driven by the unmasking of hitherto silent neurons (Figure 6 – figure supplement 1C) or increased activity rates of individual neurons over time (Kotak et al., 2005; Noreña et al., 2010; Norena et al., 2003; Seki and Eggermont, 2003a). Normalizing by the pre-exposure period, in the noise-exposed mice there was approximately a 20% increase in cellular spontaneous activity across A1 compared to tracked cells from the sham-exposed mice (**Figure 7A-B**). Unlike the increase in edge frequency tone-responsiveness, increased spontaneous activity was not topographically restricted and continued to increase steadily with time after acoustic trauma (**Figure 7B-C**).

Tinnitus and loudness hypersensitivity are thought to arise from a combination of increased activity rates as well as increased synchrony between cells (Auerbach et al., 2018, 2014; Resnik and Polley, 2021; Seki and Eggermont, 2003b; Shore and Wu, 2019). To determine how increased synchrony developed over topographic space and post-trauma time, we cross-correlated periods of spontaneous activity between pairs of A1 PyrNs and removed the influence of gross changes in activity rates through shuffle correction (**Figure 7D, see Methods**). Using the area under the shuffle-corrected cross-correlogram as our index of pairwise synchrony (**Figure 7D**), we noted that synchronized activity normally decayed to asymptote once PyrNs were separated by more than 0.25mm (**Figure 7E, top**). In the first 72 hours following acoustic trauma, pairwise synchrony was significantly enhanced for PyrNs separated by as much as 0.7mm (**Figure 7E, bottom**). Three days after trauma and beyond, synchrony remained strongly elevated for PyrNs relative both to baseline and sham-exposed controls. Increased synchrony following trauma was primarily observed in PyrN's located close to – or straddling – the deafferentation boundary, where the peak of elevated synchrony was positioned within a tonotopic region corresponding to lesion edge sound frequencies (**Figure 7F**).

Predicting the degree of excess central gain after trauma in individual PyrNs based on their pre-exposure response features

Chronic PyrN tracking brings cortical plasticity associated with acoustic trauma into sharper relief by specifying how changes unfold both in space and time at the level of single cells. It also underscores considerable heterogeneity in the expression of central gain changes between individual PyrNs. For example, for two PyrNs located within the deafferented region, one could show stable 8 kHz growth functions after trauma (**Figure 8A**) and the other excess gain (**Figure 8B**). To account for unexplained variability in central gain changes, we asked whether response features measured in the pre-exposure baseline period could predict whether neurons would express homeostatic or non-homeostatic regulation of sound-evoked activity. Returning to the same two example neurons, we noted that the PyrN that maintained stable gain had a relatively low spontaneous activity rate and sharp frequency tuning prior to acoustic trauma, whereas the PyrN that would express excess gain had higher spontaneous activity and a relatively broad pure tone receptive field (**Figure 8B-C**). Expanding this analysis to additional example neurons over post-exposure time further suggests that PyrNs that would go on to express non-homeostatic auditory growth functions tended to feature higher spontaneous activity levels at baseline (**Figure 8D**).

We used a multiple linear regression model to better capture how baseline properties can explain heterogenous changes in neural response gain. Central gain was operationally defined as the change in the area under the 8 kHz growth function relative to the PyrN's baseline growth function area (as per Figure 8A-B). Quantifying neural gain as fold change in the normalized 8 kHz growth function area recapitulated the same topographic and temporal dependence described above with intensity growth slope (**Figure 8 – figure supplement 1A**). To avoid overfitting the regression model, we selected a single timepoint - 3-5 days after noise exposure - that captured the permanent changes after acoustic trauma while maximizing our sample size of chronically tracked PyrNs. As predictor variables, we selected various spontaneous and sound-evoked response baseline features along with features related to the physical position of the PyrN within the A1 tonotopic map (see Figure 8 legend).

We found that regressing the post-exposure change in neural gain on baseline PyrN's response features could account for approximately 40% of the variance in central gain changes after acoustic trauma but just 13% in sham-exposed where neural gain changes were small overall and far less systematic (**Figure 8E**). This is noteworthy because the model excluded features related to the degree of cochlear damage or reduced bottom-up sensory afferent drive, which are traditionally interpreted as the primary determinants of cortical central gain changes. To determine the weighting of each predictor variable to the overall model fit, we randomly shuffled each variable and refit the model to calculate the decrement in the adjusted R squared. The results are provided for all of the univariate predictors (**Figure 8F)** and all predictors including interaction terms (**Figure 8 – figure supplement 1B**). We observed that excess non-homeostatic gain regulation following acoustic trauma occurred with the highest probability in PyrNs exhibiting weak, monotonically increasing 8 kHz growth functions and higher spontaneous activity levels at baseline (**Figure 8G**). Further, PyrNs located in the high-frequency (deafferented) region but with a lower frequency BF further increased the likelihood of expressing excess neural gain after trauma (**Figure 8G**). Taken together, these findings show that certain idiosyncratic response features measured just prior to

acoustic trauma can predict whether A1 L2/3 PyrNs will undergo stable, homeostatic regulation or excess, non-homeostatic changes to a stimulus positioned near the edge of the cochlear lesion.

DISCUSSION

Here, we introduced a noise exposure protocol that selectively damages sensory neurons and neural afferents in the high-frequency base of the cochlea, providing a mouse model for the common high-frequency hearing loss profile in humans that is often associated with tinnitus, loudness hypersensitivity, and poor multitalker speech intelligibility (Figure 1). We demonstrated that behavioral hypersensitivity to spared, mid-frequency tones was also observed for direct stimulation of thalamocortical projection neurons, identifying the ACtx as a potential locus of plasticity underlying loudness hypersensitivity (Figure 2). We tracked ensembles of excitatory PyrNs over several weeks and confirmed large-scale reorganization of ACtx tonotopic maps (Figure 3) and sound intensity coding (Figure 4) that recapitulated the loudness hypersensitivity documented behaviorally (Figure 5). Neural hyperreactivity to spared mid-frequency sounds was accompanied by hyperactive and hypercorrelated spontaneous activity (Figure 7), where the degree of excess neural gain following acoustic trauma in individual neurons could be predicted from many of these response features measured during the pre-exposure baseline period (Figure 8). Collectively, these findings underscore the close association between excess cortical gain and disordered sound perception after cochlear sensorineural damage and identify activity signatures that predispose neurons to non-homeostatic hyperactivity following noise-induced hearing loss.

Underlying mechanisms

Loudness recruitment is a common auditory perceptual complaint associated with sensorineural hearing loss. Loudness recruitment describes a disproportionate growth of perceived loudness with sound level, resulting in a compression of the dynamic range separating the minimal audible level and uncomfortable loudness level. Excess central gain – an abnormally steep growth of neural response with sound intensity – is the hypothesized neural substrate of loudness recruitment and generalized hyperacusis (Auerbach et al., 2018, 2014; Zeng, 2020, 2013). Excess central gain is prominently in the ACtx of animals with sensorineural cochlear damage (Asokan et al., 2018; Chambers et al., 2016a; Norena et al., 2003; Parameshwarappa et al., 2022; Popelář et al., 1987; Qiu et al., 2000; Resnik and Polley, 2021, 2017; Seki and Eggermont, 2003b; Syka et al., 1994) by contrast to the auditory nerve, where sound-evoked neural responses are strongly reduced (Heinz et al., 2005; Heinz and Young, 2004; Wake et al., 1993). Excess central gain is also observed in subcortical stations of sound processing in animals with sensorineural cochlear damage (Chambers et al., 2016b; Kamke et al., 2003; Niu et al., 2013; Schrode et al., 2018; Shaheen and Liberman, 2018), but only particular cell types (Cai et al., 2009) and – in studies that have made direct inter-regional comparisons – is less robust than neural gain changes at the level of ACtx (Chambers et al., 2016a; Qiu et al., 2000).

Our findings build upon this literature by demonstrating excess central gain in L2/3 excitatory PyrNs that resembled behavioral hypersensitivity to spared mid-frequency tones. Seminal work demonstrated that animals became behaviorally hypersensitive to electrical microstimulation of central auditory neurons following cochlear damage (Gerken, 1979). Here we expanded on this observation by demonstrating that noise-exposed mice are behaviorally hypersensitive to direct activation of thalamocortical projection neurons, which further underscores the association between excess cortical gain and sound hypersensitivity. Hypersensitivity to direct stimulation of the thalamocortical pathway may be underpinned by changes in ACtx gene expression that result in elevated mRNA levels for glutamate receptor subunits and reduced mRNA transcripts and membrane-bound protein expression for GABAA receptor units (Balaram et al., 2019; Sarro et al., 2008). These adjustments in ligand-gated receptors have been associated with commensurate elevations in spontaneous excitatory postsynaptic currents and reduced inhibitory postsynaptic currents in PyrNs (Kotak et al., 2005; S. Yang et al., 2011). Thus, disinhibition and hypersensitization are conceptualized as synergistic compensatory responses that are triggered by a sudden decline in peripheral neural input, rendering cortical PyrNs less sensitive to feedforward inhibition from local inhibitory neurons – from parvalbumin-expressing (PV) fast-spiking interneurons in particular – and hyper-responsive to sound (Masri et al., 2021; Resnik and Polley, 2021, 2017).

One challenge to this purely bottom-up model for compensatory plasticity underlying excess central gain is that it cannot readily account for why neighboring neurons can exhibit such heterogenous changes in sound-evoked hyperresponsivity after peripheral damage. Here, we found that approximately 40% of the variability in excess central gain among individual PyrNs could be accounted for by their response properties measured in the days just prior to acoustic trauma. In particular, PyrNs with low spontaneous activity rates and greater responses to low-intensity tones – features associated with stronger intracortical inhibition (Tan et al., 2007; Wu et al., 2006) – showed more stable gain control after trauma. Conversely, PyrNs with response features suggesting weaker baseline inhibition showed the strongest excess gain after trauma.

Several recent findings support the idea that variations in the strength of intracortical inhibition can function as a watershed to produce dichotomous functional outcomes. In an earlier study, we applied ouabain to the cochlear round window to produce bilateral lesions of approximately 95% of cochlear afferent neurons. Near-complete elimination of cochlear afferent input was associated with functional deafness at the level of the ACtx in approximately half the animals but a remarkable recovery of sound responsiveness in the other half. Single unit recordings from the cohort of mice that recovered sound processing weeks after cochlear neural loss all featured a rapid decline in PV-mediated feedforward inhibition onto PyrNs during the first hours and days following the peripheral injury, while the mice that showed no functional recovery expressed a far slower decay in PV-mediated inhibition (Resnik and Polley, 2017). Another piece of evidence comes from ACtx single unit recordings in marmosets outfitted with unilateral cochlear implants. Single units with narrowly tuned, non-monotonic frequency response areas – presumably reflecting stronger local inhibition – were suppressed by spatially diffuse electrical stimulation of the auditory nerve, while units

with broad, V-shaped selectivity encoded cochlear input stimulation with high fidelity (Johnson et al., 2016). Collectively, these findings underscore that the effects of peripheral injury on central circuits are not exclusively determined by bottom-up drive but instead are also brokered by variations in the balance of excitation and inhibition within the local circuit or gene expression differences between individual cells. At a global level, these mitigating influences are shaped by developmental stage (Dorrn et al., 2010; Harris et al., 2005; Sun et al., 2011) and circadian programs (Basinou et al., 2017), but – at the level of individual neurons – may reflect latent differences in genetic subtypes of L2/3 PyrNs or purely stochastic variations in inhibitory tone between different microcircuit milieus.

Behavioral hypersensitivity: interpretations and technical limitations

We found evidence of behavioral hypersensitivity to sound following acoustic trauma as measured by a steeper relationship between increasing tone intensity and detection ability in our Go/NoGo task (Figure 2). Although previous indicators of loudness sensitivity in animals have relied on more reflexive measures, such as the acoustic startle response (Hickox and Liberman, 2014; Sun et al., 2012), more recent work has utilized operant detection tasks including reaction times as an approximation of sound hypersensitivity (Auerbach et al., 2018). Here, we used a modified 2-up, 1 down design such that mice perform the task primarily near their perceptual threshold, where there is a large dynamic range to measure changes in task performance. Furthermore, to control for any changes in licking behavior due to acoustic trauma, our slope measurements are taken from functions using a sensitivity index (d'), which normalizes lick probability according to the false alarm rate determined from the delivery of catch (silent) trials. Thus, a steeper relationship between increasing tone intensity and perceptual sensitivity strongly suggests a hypersensitivity to sound following acoustic trauma (Figure 2).

Hyperacusis describes a spectrum of aversive auditory qualities including increased loudness of moderate intensity sounds, a decrease in loudness tolerance, discomfort, pain, and even fear of sounds (Pienkowski et al., 2014a). The affective components of hyperacusis are more challenging to index in animals, particularly head-fixed behaviors, though progress is being made with active avoidance paradigms in freely moving animals (Manohar et al., 2017). Our evidence of hypersensitivity is likely more reflective of the sensory component of hyperacusis: an increase in perceived loudness relative to pre-exposure performance or mice that have not undergone acoustic trauma.

Measures of loudness perception in humans rely on various tasks, such as cross-modality matching, categorical loudness assessment, and simple magnitude estimation (Marozeau and Florentine, 2007). Go/NoGo detection behaviors do not accomplish the same direct assessment of loudness captured by these tasks, and instead rely on the average performance across tens or hundreds of trials in order to assemble a detection function. Instead, an operant behavior in which single trials directly assess loudness perception would prove extremely useful in animal studies of hearing loss and sound sensitivity, but such a task would require a more complicated design and training regimen (Alkharabsheh et al., 2017). Although many accumulated trials are necessary, we were able to acquire a detection function that approximates a

loudness growth function. By design, we focused our behavioral measurements on sound levels near threshold, to demonstrate loudness hypersensitivity at physical intensities far below the range implicated in cochlear loudness recruitment following OHC damage. Furthermore, our measured steepening of detection functions following noise exposure closely resembles theoretical altered loudness growth curves in models of hyperacusis (Zeng, 2020, 2013), underscoring the validity of our approach despite its simplicity.

Cortical hyperreactivity: interpretations and technical limitations

Two-photon calcium imaging offers several key advantages for cortical plasticity studies including the ability to track single neurons over weeks (Figure 6) and genetic access to multiple cell types (Resnik and Polley, 2021). On the other hand, it can provide less insight into the mechanisms underlying destabilized excitatory-inhibitory balance than electrophysiological approaches (Resnik and Polley, 2017; S. Yang et al., 2011; Yang et al., 2012). Further, calcium indicators provide an approximation of neural activity and can be limited in their kinetics and reliability to report precise cellular events (Grienberger and Konnerth, 2012), although correct deconvolution and post-hoc analysis techniques can help to minimize issues introduced from calcium imaging (Sabatini, 2019).

Homeostatic Plasticity describes a negative feedback process that stabilizes neural activity levels following input perturbations. Homeostatic Plasticity mechanisms modify excitatory and inhibitory synapses over a period of hours or days to offset input perturbations and gradually restore spiking activity back to baseline levels (Turrigiano, 2012, 2008). Importantly, cytosolic calcium is itself the upstream barometer of activity that regulates the molecular signaling cascades underlying AMPA receptor scaling or GABA receptor removal (Harris and Rubel, 2006; Turrigiano, 2012). This underscores a key advantage to using calcium imaging in experiments that monitor network activity following perturbations of peripheral input levels: that although GCaMP is a closely related but indirect measure of spiking, it arguably provides more direct insight than spiking into the key upstream signal driving Homeostatic Plasticity signaling cascades.

Although we did not measure Homeostatic Plasticity per se, via direct demonstrations of intrinsic or heterosynaptic electrophysiological changes, our measurements of spontaneous and sound-evoked calcium transients clearly demonstrate a failure of homeostatic regulation following acoustic trauma. Spontaneous and sound-evoked calcium levels both remained elevated above pre-exposure baseline levels or levels observed in sham-exposed control mice. Hyperactive and hyper-correlated activity in regions of the cortical topographic map corresponding to peripheral sensorineural damage is widely understood to be the underlying neural basis of phantom sound perception in tinnitus. Here, we show that these changes are also a likely underlying neural substrate for auditory hypersensitivity, a core component of hyperacusis that often accompanies tinnitus (Cederroth et al., 2020; Schecklmann et al., 2014). These findings identify a neurophysiological target for testing therapeutic strategies in animals and inform the selection of non-invasive biomarkers for the development of improved diagnostics and therapies in human populations (Polley and Schiller, 2022).

MATERIALS AND METHODS

Key Resources Table

Reagent Type	Designation	Source or Reference	Identifiers	Additional Information
Genetic reagent (*Mus musculus*)	C57BL/6J-Tg(Thy1-GCaMP6s)GP4.12Dkim/J	Jackson Laboratory	JAX #025776	Male
Genetic reagent (*Mus musculus*)	CBA/CaJ	Jackson Laboratory	JAX #000654	Female
Genetic reagent (*Mus Musculus*)	C57BL/6J	Jackson Laboratory	JAX #000664	Male/Female
Recombinant DNA reagent	AAVrg-pgk-Cre	Addgene	Addgene #24593-AAVrg	
Recombinant DNA reagent	AAV5-Ef1a-DIO hChR2(E123T/T159C)-EYFP	Addgene	Addgene #35509-AAV5	
Antibody	ms(1gG1) α CtBP2	BD Transduction Labs	BDB612044	1:200
Antibody	rb α MyosinVIIa	Proteus Biosciences	25-6790	1:200
Antibody	ms(1gG2a) α GluA2	Millipore	MAB397	1:2000
Antibody	rb α Epsin	Sigma	HPA028674	1:100
Antibody	gt α ms (IgG2a) AF 488	Thermo Fisher	A-21131	1:1000
Antibody	gt α ms (IgG1) AF 568	Thermo Fisher	A-21124	1:1000
Antibody	dk α rb AF 647	Thermo Fisher	A-31573	1:200
Antibody	gt α rb PacBlue	Thermo Fisher	P10994	1:200
Chemical compound, drug	Lidocaine hydrochloride	Hospira Inc	Cat #71-157-DK	
Chemical compound, drug	Buprenorphine hydrochloride	Buprenex	Cat #NDC 12496-0757-5	
Chemical compound, drug	Isoflurane	Piramal	Cat #NDC 66794-013-10	
Chemical compound, drug	Silicon adhesive	WPI	Cat #KWIK-SIL	
Chemical compound, drug	C&B Metabond Quick Adhesive Cement System	Parkwell	Cat #S380	
Software, algorithm	Labview	National Instruments	https://www.ni.com/en-us/shop/labview.html	Version 2015
Software, algorithm	ThorImage 3.0	Thorlabs	https://www.thorlabs.com/newgrouppage9.cfm?objectgroup	
Software, algorithm	Suite2P	Github	https://github.com/cortex-lab/Suite2P	
Software, algorithm	CellReg	Github	https://github.com/zivlab/CellReg	
Software, algorithm	MATLAB	Mathworks	https://www.mathworks.com/products/matlab.html	Version 2017b
Other	Solenoid driver	Eaton-Peabody Labs	https://github.com/EPL-Engineering/epl_valve	

Other	Lickometer	Eaton-Peabody Labs	https://github.com/EPL-Engineering/epl_lickometer	
Other	PXI Controller	National Instruments	PXIe-8840	
Other	Free-field speaker	Parts Express	275-010	
Other	Ti-Sapphire Laser	Spectra Physics	Mai Tai HP DeepSee	
Other	16x/.8NA Objective	Nikon	CFI75 LWD 16X W	
Other	Two-Photon Microscope	Thorlabs	Bergamo II	
Other	Titanium headplate	iMaterialise	Custom	
Other	Diode laser (488 nm)	Omnicron	LuxX 488-100	

EXPERIMENTAL MODEL AND SUBJECT DETAILS

All procedures were approved by the Massachusetts Eye and Ear Animal Care and Use Committee and followed the guidelines established by the National Institute of Health for the care and use of laboratory animals. Imaging and tone Go/NoGo behavior were performed on Thy1-GCaMP6s x CBA mice. Combined acoustic and optogenetic Go/NoGo behavioral studies were performed in C57BL/6J mice. Mice of both sexes were used for this study. Mice were noise- or sham-exposed in the morning at 9 weeks postnatal. Mice were maintained on a 12 hr light/12 hr dark cycle. Mice were provided with *ad libitum* access to food and water unless they were on-study for behavioral testing, in which case they had restricted access to water in the home cage.

Data were collected from 44 mice. A total of 22 mice contributed data to behavioral tasks: 13 (N = 7/6, trauma/sham) to the tone Go/NoGo behavior and 9 (N = 6/3, trauma/sham) to the combined acoustic and optogenetic Go/NoGo behavior. A total of 10 mice contributed to the chronic imaging experiments: Two mice were used for widefield imaging (N = 1/1, trauma/sham) and 8 (N = 4/4, trauma/sham) to the two-photon imaging. Twelve mice were only used for regular ABR testing after acoustic trauma to determine the progression of threshold shift. Cochlear histology was performed on 11 of the mice used for Go/NoGo behavioral testing (N = 7/4, trauma/sham).

METHOD DETAILS

Survival surgeries for awake, head-fixed experiments

Mice were anesthetized with isoflourane in oxygen (5% induction, 1.5%–2% maintenance). A homeothermic blanket system was used to maintain body temperature at 36.6 (FHC). Lidocaine hydrochloride was administered subcutaneously to numb the scalp. The dorsal surface of the scalp was retracted and the periosteum was removed. The skull surface was prepped with etchant and 70% ethanol before affixing a titanium head plate to the dorsal surface with dental cement. At the conclusion of the headplate attachment and any additional procedures listed below, Buprenex (0.05 mg/kg) and meloxicam (0.1 mg/kg) were administered, and the animal was transferred to a warmed recovery chamber.

High-frequency noise exposure

To induce acoustic trauma, octave-band noise at 16-32 kHz was presented at 103 dB SPL for 2 hours. Exposure stimulus was delivered via a tweeter fixated inside a custom-made exposure chamber (51 × 51 × 51 cm). The interior walls of the acoustic enclosure joined at irregular, non-right angles to minimize standing waves. Additionally, to further diffuse the high-frequency sound field, irregular surface depths were achieved on three of the interior walls by attaching stackable ABS plastic blocks (LEGO). Prior to exposure, mice were placed, unrestrained, in an independent wire-mesh chamber (15 × 15 × 10 cm). This chamber was placed at the center of a continuously rotating plate, ensuring mice were exposed to a relatively uniform sound field. Sham-exposed mice underwent the same procedure except that the exposure noise was presented at an innocuous level (40 dB SPL).

Go/NoGo tone detection task

Three days after headplate surgery, animals were weighed and placed on a water restriction schedule (1 mL per day). During behavioral training, animals were weighed daily to ensure they remained between 80-85% of their initial weight and regularly examined for signs of excess dehydration. Mice were given supplemental water if they received less than 1 mL during a training session or appeared excessively dehydrated. During testing, mice were head-fixed in a dimly lit, single-walled sound attenuating booth (ETS-Lindgren), with their bodies resting in an electrically conductive cradle. Tongue contact on the lickspout closed an electrical circuit that was digitized (at 40 Hz) and encoded to calculate lick timing. Digital and analog signals controlling sound delivery and water reward were controlled by a PXI system with custom software programmed in LabVIEW. Free-field stimuli were delivered via an inverted dome tweeter positioned 10 cm from the left ear and calibrated with a wide-band ultrasonic acoustic sensor (Knowles Acoustics).

Most mice required two weeks of behavioral shaping before they could perform the complete tone detection task with psychophysical staircasing. After mice were habituated to head-fixation, they were conditioned to lick the spout within 2 s following the onset of an 8 or 32 kHz 70 dB SPL tone (0.25 s duration, with 5ms raised cosine onset-offset ramps) to receive a small quantity of water (4 μL). Trials had a variable inter-trial interval (4-10 s) randomly selected from a truncated exponential distribution. Once reaction times were consistently < 1 s, mice were trained to detect 8 kHz and 32 kHz tones in a 2-down, 1-up adaptive staircasing paradigm, where two correct detections were required to decrease the range of sound intensities by 5 dB SPL and one miss was required to increase the range of sound intensities by 5 dB SPL. At each iteration of the adaptive staircasing procedure, three trials were presented: a catch (silent) trial and tones at +/- 5 dB SPL relative to the last intensity tested (Figure 1I). A single frequency was presented until 1 reversal was reached, and then the other tone was presented; a run was completed once 6 reversals had been reached for both frequencies. The first frequency presented each run was randomized.

Hits were defined as post-target licks that occurred > 0.1 s and < 1.5 s following the onset of the target tone. False alarms (Go responses on a catch trial) triggered a 5 s time out. Entire runs were excluded from analysis if the false alarm rate was greater than 30%. This exclusion criterion resulted in the elimination of < 5% of test runs across all conditions (before, after, noise- or sham-exposure), underscoring that mice were under stimulus control even if their hearing thresholds were elevated. Psychometric functions were fit using binary logistic regression. Threshold was defined as the average intensity at reversals across an entire session.

Go/NoGo optogenetic detection task

Headplate attachment, anesthesia and analgesia followed the procedure described above. Three burr holes were made in the skull over auditory cortex (1.75 – 2.25mm rostral to the lambdoid suture). We first expressed Cre-recombinase in neurons that project to the ACtx by injecting 150 nL of AAVrg-pgk-Cre 0.5mm below the pial surface at three locations within the ACtx with a precision injection system (Nanoject III) coupled to a stereotaxic positioner (Kopf). A fourth injection was then performed to selectively express channelrhodopsin in auditory thalamocortical projection neurons by injecting 100 nL of AAV5-Ef1a-DIO hChR2(E123T/T159C)-EYFP in the MGBv (-2.95mm caudal to bregma, 2.16mm lateral to midline, 3.05mm below the pial surface). An optic fiber (flat tip, 0.2mm diameter, Thorlabs) was inserted at the MGB injection coordinates to a depth of 2.9mm below the pial surface. The fiber assembly was cemented in place and painted with black nail polish to prevent light leakage. Animals recovered for at least three days before water restriction and behavioral testing began.

After mice were habituated to head-fixation, they were conditioned to lick the spout within 2 s following the onset of 70 dB SPL high frequency bandpass noise (centered at 32 kHz, width 1 octave). Once consistent, mice were trained to detect optogenetic activation of thalamocortical neurons. The laser was pulsed at 10Hz, 10ms pulse width for 500ms, and the bandpass noise was pulsed at 10Hz, 20ms pulse width (5ms raised cosine onset-offset ramps) for 500 ms. For testing, randomized interleaved blocks of either noise or laser stimulation were presented at a range of levels, including catch trials. The range of sound levels and laser powers were tailored to each mouse prior to noise exposure to ensure equivalent sampling of sound and laser perceptual growth functions. We first defined the lowest laser power and sound level that produced at least 95% hit rates (operationally defined as “max”). Sound levels and laser powers were then presented at six attenuated levels relative to the maximum per day in each mouse. Psychometric functions were fit using binary logistic regression, and threshold was defined as the closest point where the

Go (lick) probability was equal to 50%. Runs were rejected for further analysis if the false alarm rate of the mouse was above 30%, and again this resulted in the exclusion of <5% of sessions.

Widefield and two-photon calcium imaging

Three round glass coverslips (two 3mm and one 4mm diameter, #1 thickness, Warner Instruments) were etched with piranha solution and bonded into a vertical stack using transparent, UV-cured adhesive (Norland Products, Warner Instruments). Headplate attachment, anesthesia and analgesia follow the procedure listed above. A circular craniotomy (3mm diameter) was made over the right ACtx using a scalpel and the coverslip stack was cemented into the craniotomy. Animals recovered for at least 5 days before beginning imaging recordings. All imaging was performed in awake, passively listening animals.

A series of pilot widefield imaging experiments were performed to visualize changes in all fields of the ACtx over a longer, 30–60-day post-exposure time period (N= 8 noise-exposed and 7 sham-exposed mice). The data collection procedure for these pilot experiments followed the methods described in detail in our previous publication (Romero et al., 2019). Briefly, widefield epifluorescence images were acquired with a tandem-lens microscope (THT-microscope, SciMedia) configured with low-magnification, high-numerical aperture lenses (PLAN APO, Leica, 2× and 1× for the objective and condensing lenses, respectively). Blue illumination was provided by a light-emitting diode (465 nm, LEX2-LZ4, SciMedia). Green fluorescence passed through a filter cube and was captured at 20Hz with a sCMOS camera (Zyla 4.2, Andor Technology).

Cellular imaging was performed with a 2-photon imaging system in a light-tight sound-attenuating enclosure mounted on a floating table (Bergamo II Galvo-Resonant 8 kHz scanning microscope, Thorlabs). An initial lower resolution epifluorescence widefield imaging session was performed with a CCD camera to visualize the tonotopic gradients of the ACtx and identify the position of A1 (as shown in Figure 3C). Two-photon excitation was provided by a Mai-Tai eHP DS Ti:Sapphire-pulsed laser tuned to 940 nm (Spectra-Physics). Imaging was performed with a 16×/0.8NA water-immersion objective (Nikon) from a 512 × 512 pixel field of view at 30Hz with a Bergamo II Galvo-Resonant 8 kHz scanning microscope (Thorlabs). Scanning software (Thorlabs) was synchronized to the stimulus generation hardware (National Instruments) with digital pulse trains. The microscope was rotated by 50-60 degrees off the vertical axis to obtain images from the lateral aspect of the mouse cortex while the animal was maintained in an upright head position. Animals were monitored throughout the experiment to confirm all imaging was performed in the awake condition using modified cameras (PlayStation Eye, Sony) coupled to infrared light sources. Imaging was performed in layers L2/3, 175-225 mm below the pial surface. Fluorescence images were captured at 1× digital zoom, providing an imaging field of 0.84 × 0.84 mm.

Raw calcium movies were processed using Suite2P, a publicly available two-photon calcium imaging analysis pipeline (Pachitariu et al., 2016). Briefly, movies are registered to account for brain motion. Regions of interest are established by clustering neighboring pixels with similar time courses. Manual curation is then performed to eliminate low-quality or non-somatic regions of interest. Spike deconvolution was also performed in Suite2P, using the default method based on the OASIS algorithm (Friedrich et al., 2017). For chronic tracking of individual cells across imaging sessions, cross-day image registration was performed using a method outlined by Sheintuch et al (Sheintuch et al., 2017). Briefly, fields-of-view are aligned to a reference imaging session using a non-rigid transformation, and a probabilistic modeling approach is used to estimate whether neighboring cells from separate sessions are the same or different cells. To estimate the false positive rate with this approach, we also performed a control in which cross-day registration was performed with daily imaging fields randomly selected from different mice (Figure 6 – Figure Supplement 1). For all analysis of tracked neurons, only cells with a confidence score of at least 0.8 (max of 1) and that were tracked for at least 8 of the 15 imaging sessions were used for the analysis.

During widefield imaging sessions, 20-70 dB SPL tones (in 10 dB steps) were presented from 4-64 kHz in 0.5 octave steps. On the first and last two-photon imaging sessions and on the day of noise exposure, 20-80 dB SPL tones (15 dB steps) were presented from 4-45.3 kHz (0.5 octave steps). For all other two-photon imaging sessions, 20-80 dB SPL tones (in 10 dB steps) were presented at 5.7, 8, 11.3, and 32 kHz. Each day, all stimuli were repeated 20 times. One block consisted of all frequency-intensity combinations, and stimuli were randomized within blocks. Tones were 50 msec with 5ms raised cosine onset-offset ramps with 3s inter-trial intervals.

Cochlear function tests

Animals were anesthetized with ketamine (120 mg/kg) and xylazine (12 mg/kg), were placed on a homeothermic heating blanket during testing, with half the initial ketamine dose given as a booster when required. Acoustic stimuli were presented via in-ear acoustic assemblies consisting of two miniature dynamic earphones (CUI CDMG15008–03A) and an electret condenser microphone (Knowles FG-23339-PO7) coupled to a probe tube. Stimuli were calibrated in the ear canal in each mouse before recording. ABR stimuli were 5 ms tone pips at 8,12,16 or 32 kHz with a 0.5 ms rise-fall time delivered at 30 Hz. Intensity was incremented in 5 dB steps, from 20 to 100 dB SPL. ABR threshold was defined as the lowest stimulus level at which a repeatable waveform could be identified. DPOAEs were measured in the ear canal using primary tones with a frequency ratio of 1.2, with the level of the f2 primary set to be 10 dB less than f1 level, incremented together in 5 dB steps. The 2f1-f2 DPOAE amplitude and surrounding noise floor were extracted. DPOAE threshold was defined as the lowest of at least two continuous f2 levels, for which the DPOAE amplitude was at least two standard deviations greater than the noise floor. DPOAE and ABR testing was performed one week before noise- or sham-exposure, and again immediately following the conclusion of behavioral testing or imaging.

Cochlear histology

To visualize cochlear afferent synapses and inner- and outer- hair cells, cochleae were dissected and perfused through the round window and oval window with 4% paraformaldehyde in phosphate-buffered saline, then post-fixed in the same solution for 1 hour. Cochleae were then decalcified in 0.12M EDTA for 2 days and dissected into half-turns for whole-mount processing. Immunostaining began with a blocking buffer (PBS with 5% normal goat or donkey serum and 0.2-1% Triton X-100) for 1 hour at room temperature. Whole mounts were then immunostained by incubating with a combination of the following primary antibodies: 1) rabbit anti-CtBP2 at 1:100, 2) rabbit anti-myosin VIIa at 1:200, 3) mouse anti-GluR2 at 1:2,000 and secondary antibodies coupled to the red, blue, and green channels. Immunostained cochlear pieces were measured, and a cochlear frequency map was computed (Müller et al., 2005) to associate structures to relevant frequency regions using a plug-in to ImageJ (Parthasarathy and Kujawa, 2018).

Images were collected at 2400x900 raster using a using a high-resolution, oil immersion objective (63x, numerical aperture 1.3), and 1.25x zoom and assessed for signs of damage. Confocal z-stacks at identical frequencies were collected using a Leica TCS SP5 microscope to visualize hair cells and synaptic structures. Two adjacent stacks were obtained (78 um cochlear length per stack) at each target frequency spanning the cuticular plate to the synaptic pole of ~10 hair cells (in 0.25 um z-steps). Images were collected in a 1024 x 512 raster using a high-resolution, oil immersion objective (63x, numerical aperture 1.3), and digital zoom (3.17x). Images were loaded into an image-processing software platform (Amira; VISAGE Imaging), where IHCs were quantified based on their Myosin VIIa-stained cell bodies and CtBP2-stained nuclei. Presynaptic ribbons and postsynaptic glutamate receptor patches were counted using 3D representations of each confocal z-stack. Juxtaposed ribbons and receptor puncta constitute a synapse, and these synaptic associations were determined by calculating and displaying the x–y projection of the voxel space within 1 um of each ribbon's center(Liberman et al., 2011). OHCs were counted based on the myosin VIIa staining of their cell bodies. The mean number of cells per row of OHCs was used as a measure of OHC counts.

For visualizing OHC stereocilia damage, following similar whole-mount dissection and blocking procedures, the other ear was immunostained with a combination of the following primary antibodies 1) rabbit anti-CtBP2 at 1:100, 2) mouse anti-GluR2 at 1:2,000 and 3) rabbit anti-Espin at 1:100, followed by secondary antibodies in the red, green and gray channels. Confocal z-stacks of the stereocilia were collected at 5.6, 11.3, 22, 32, 45, and 64 kHz cochlear frequencies with a Leica TCS SP8 microscope.

Brain histology

For mice performing the Go/NoGo optogenetic detection task, at the conclusion of behavioral testing mice were deeply anesthetized and prepared for transcardial perfusion with a 4% formalin solution in 0.1M phosphate buffer. The brains were extracted and post-fixed at room temperature for an additional 12 hours before transfer to 30% sucrose solution. Coronal sections (50um) were mounted onto glass slides using Vectashield with DAPI, and then coverslipped. Regions of interest were then imaged at 10x using a Leica DM5500B fluorescent microscope.

QUANTIFICATION AND STATISTICAL ANALYSIS

Clinical database analysis

First-visit patient records from the Massachusetts Eye and Ear audiology database over a 24-year period from 1993 to 2016 were analyzed. Our analysis selected for adult patients aged 18 and 80, whose primary language was English, and who underwent pure tone audiogram tests in the left and right ears with octave spaced frequencies between 250Hz – 8 kHz using headphones or inserts. To eliminate patients with conductive components in their hearing loss, the MEE dataset was further curated to remove all audiograms where the air-bone gap was ≥20 dB at any one frequency or ≥15 dB at two consecutive frequencies. Audiograms with thresholds ≥85 dB HL at frequencies ≤2000 Hz were also removed to maintain a conservative inclusion criterion, as the difference in limits of the air and bone conducting transducers limit our ability to determine the presence of conductive components in that threshold range. After this exclusionary step, we were left with 132,504 audiograms in the dataset for analysis. Of these audiograms, HFHL was defined as audiograms with thresholds lower than 20dB HL for frequencies < 1kHz, between 10 and 80dB HL for 2 kHz, between 20 and 120 dB HL for 4 kHz, and between 40 and 120dB HL for 8 kHz, following the same criteria used to identify a steeply sloping high frequency hearing loss in prior clinical database studies (Dubno et al., 2013; Parthasarathy et al., 2020b; Vaden et al., 2017). HFHL audiometric phenotypes consisted of 23% of the audiograms assessed based on these criteria. These patients were 65% male and had a median age of 65 years. The study was approved by the human subjects Institutional Review Board at Mass General Brigham and Massachusetts Eye and Ear. Data analysis was performed on de-identified data, in accordance with the relevant guidelines and regulations.

Behavioral Analysis

To estimate perceptual gain in the Go/NoGo tone detection task, hit rates were taken at intensities ranging from the lowest intensity with sufficient trials (>5 trials) to the first intensity at which the hit rate was above 90% to account for saturation of the detection function. The perceptual gain was calculated as the average first derivative of the d' function evaluated over the specified intensity range. The gain calculation was performed for each animal based on aggregated daily test sessions for a given post-exposure epoch (e.g., baseline, 0-2 days post-exposure).

Two-photon image analysis

All analysis was performed on the deconvolved calcium activity traces. For analysis of tone-evoked responses, averaged deconvolved calcium traces were expressed as Z-score units relative to activity levels measured during the pre-stimulus period (833 ms). PyrNs were operationally defined as being responsive to a particular tone frequency/level combination with a Z > 2. For the three imaging sessions that calculated the full frequency response area, the minimum response threshold was defined for each PyrN as the lowest level at which there were responses to two adjacent frequencies (frequencies 0.5 octaves apart). Best frequency (BF) was defined as the frequency for which the overall response was maximal over the intensity range of threshold +30 dB. Analysis of BF changes were limited to PyrNs with pure tone receptive fields (neural d' > 1, as defined in Romero et al., 2019)).

To delineate the intact and deafferented regions of the imaging field, a support vector machine (SVM) was calculated for each mouse using BF's determined from the first day of imaging prior to noise exposure. The SVM deafferentation boundary categorized physical space (intact: BF < 16 kHz, deafferented: BF ≥ 16 kHz) and its physical location was then imposed on all successive imaging sessions after alignment of fields-of-view from all imaging sessions. To categorize the position of a neuron, the adjusted centroid locations were used based on the best registration from the previously mentioned method. The distance of a neuron to the SVM deafferentation boundary was calculated as the shortest Euclidean distance.

Gain was defined as the relationship between sound level (input) and activity rate (output). The gain was calculated as the average rate of change over a range of sound levels. The particular set of sound levels selected for gain analysis was determined according to whether the best level occurred at low, mid, or high sound levels as illustrated in Figure 5 – Figure Supplement 1. For a neuron to be considered for an analysis of gain, it was required to have a significant response (Z > 2) to at least 3 consecutive intensities.

Spontaneous activity was calculated from the 833 ms periods preceding tone onset. To quantify the correlated activity between cells, we cross-correlated the z-scored activity in the pre-stimulus periods. To control for the effects of overall changes in activity rates over sessions or between cells, shuffled cross-correlograms were generated for each pair by shuffling trial labels. Only cross-correlograms for which at least 3 consecutive lags had values significantly greater than the shuffled cross-correlogram (bootstrapped $p < 0.05$, Bonferroni corrected for multiple comparisons) were used for analysis. The degree of correlated activity between each pair was defined as the size of the positive area under the peak of the shuffle-subtracted cross-correlogram (xcorr area).

To determine how ensemble activity decoded tone presence, we used an SVM classifier with a linear kernel (following the approach of Resnik and Polley, 2021). The SVM was run on the principal components of a data matrix consisting of the z-scored responses to single tone presentations or silent periods. PCA was used to reduce the influence of any inequities in sample sizes across mice or conditions. We ran the SVM on the minimum number of principal components required to explain 90% of the variance. Leave-one-out cross-validation was then used to train the classifier and compute the decoder accuracy. We repeated this process independently for each frequency intensity at 8 and 32kHz for each imaging session. The models were fit using the 'fitcsvm' function in MATLAB.

To model how pre-exposure properties can predict the change in a neuron's responsiveness, the outcome variable was the post/pre-exposure ratio of the areas under the intensity-response growth function, where post was drawn from days 3-5 after exposure. All predictor variables were computed as average values from the pre-exposure period. The best linear model was fit using stepwise multiple linear regression using the Akaike information criterion. For the purposes of comparison, the predictor variables from the trauma model were applied to the sham model. The stepwise regression was fit using 'stepwiselm' and subsequent model fits used 'fitlm' in MATLAB.

Statistical analysis

All statistical analyses were performed in MATLAB 2017b (Mathworks). Data are reported as mean ± SEM unless otherwise indicated. Post hoc pairwise comparisons were adjusted for multiple comparisons using the Bonferroni correction.

Acknowledgements

These studies were supported by a grant from the Nancy Lurie Marks Family Foundation (DP and AT), NIH grant DC009836 (DP), DC015857 (DP and SK), DC018353 (AT), and NIH fellowship DC018974-02 (MM) and DC014871 (AH).

MM collected and analyzed all 2-photon calcium imaging data. MM, DC, and YW collected behavioral data with analysis by MM and pilot studies by KC. MM and AH collected widefield calcium data. MM and AH collected and analyzed ABR and DPOAE data. AP performed the human database analysis as well as cochlear histology analysis with guidance from SK. KH programmed the software for behavioral data collection. AH and KH developed the hardware and software for high-frequency noise exposure, with guidance from SK. DP, AT, KH, SK, AH, and MM designed the experiments. DP, MM, AH, and AP prepared the figures. DP and MM wrote the manuscript, with input from all authors.

We thank MC Liberman and A Indzhykulian for their assistance with hair cell stereocilia imaging.

Competing interests

The authors declare that no competing interests exist.

References

Alkharabsheh A, Xiong F, Xiong B, Manohar S, Chen G, Salvi R, Sun W. 2017. Early age noise exposure increases loudness perception - A novel animal model of hyperacusis. *Hearing Research* **347**:11–17. doi:10.1016/j.heares.2016.06.018

Allen PD, Eddins DA. 2010. Presbycusis phenotypes form a heterogeneous continuum when ordered by degree and configuration of hearing loss. *Hearing Research* **264**:10–20. doi:10.1016/j.heares.2010.02.001

Arciniegas, MD D, Adler, MD L, Topkoff J, Cawthra, RN E, Filley, MD CM, Reite, MD M. 1999. Subject Review: Attention and memory dysfunction after traumatic brain injury: cholinergic mechanisms, sensory gating, and a hypothesis for further investigation. *Brain Injury* **13**:1–13. doi:10.1080/026990599121827

Asokan MM, Williamson RS, Hancock KE, Polley DB. 2018. Sensory overamplification in layer 5 auditory corticofugal projection neurons following cochlear nerve synaptic damage. *Nature Communications* **9**. doi:10.1038/s41467-018-04852-y

Auerbach BD, Gritton HJ. 2022. Hearing in Complex Environments: Auditory Gain Control, Attention, and Hearing Loss. *Front Neurosci* **16**:799787. doi:10.3389/fnins.2022.799787

Auerbach BD, Radziwon K, Salvi R. 2018. Testing the Central Gain Model: Loudness Growth Correlates with Central Auditory Gain Enhancement in a Rodent Model of Hyperacusis. *Neuroscience*. doi:10.1016/j.neuroscience.2018.09.036

Auerbach BD, Rodrigues P V., Salvi R. 2014. Central gain control in tinnitus and hyperacusis. *Frontiers in Neurology* **5**:206–227. doi:10.3389/fneur.2014.00206

Bacon SP, Oxenham AJ. 2004. Psychophysical Manifestations of Compression: Hearing-Impaired Listeners In: Bacon SP, Fay RR, Popper AN, editors. Compression: From Cochlea to Cochlear Implants, Springer Handbook of Auditory Research. New York: Springer-Verlag. pp. 107–152. doi:10.1007/0-387-21530-1_4

Balaram P, Hackett TA, Polley DB. 2019. Synergistic transcriptional changes in AMPA and GABA A receptor genes support compensatory plasticity following unilateral hearing loss. *Neuroscience* **407**:108–119. doi:10.1016/j.neuroscience.2018.08.023

Basinou V, Park J sub, Cederroth CR, Canlon B. 2017. Circadian regulation of auditory function. *Hearing Research* **347**:47–55. doi:10.1016/j.heares.2016.08.018

Boyen K, Baskent D, van Dijk P. 2015. The Gap Detection Test: Can It Be Used to Diagnose Tinnitus? *Ear and Hearing* **36**:e138. doi:10.1097/AUD.0000000000000156

Brozoski TJ, Bauer CA. 2016. Animal models of tinnitus. *Hearing Research* **338**:88–97. doi:10.1016/j.heares.2015.10.011

Cai S, Ma W-LD, Young ED. 2009. Encoding intensity in ventral cochlear nucleus following acoustic trauma: implications for loudness recruitment. *JARO* **10**:5–22. doi:10.1007/s10162-008-0142-y

Campolo J, Lobarinas E, Salvi R. 2013. Does tinnitus “fill in” the silent gaps? *Noise and Health* **15**:398. doi:10.4103/1463-1741.121232

Cederroth CR, Lugo A, Edvall NK, Lazar A, Lopez-Escamez J-A, Bulla J, Uhlen I, Hoare DJ, Baguley DM, Canlon B, Gallus S. 2020. Association between Hyperacusis and Tinnitus. *J Clin Med* **9**. doi:10.3390/jcm9082412

Chambers AR, Resnik J, Yuan Y, Whitton JP, Edge AS, Liberman MC, Polley DB. 2016a. Central gain restores auditory processing following near-complete cochlear denervation. *Neuron* **89**:1–13. doi:10.1016/j.neuron.2015.12.041

Chambers AR, Salazar JJ, Polley DB. 2016b. Persistent thalamic sound processing despite profound cochlear denervation. *Frontiers in Neural Circuits* **10**:1–13. doi:10.3389/fncir.2016.00072

Chen T-W, Wardill TJ, Sun Y, Pulver SR, Renninger SL, Baohan A, Schreiter ER, Kerr RA, Orger MB, Jayaraman V, Looger LL, Svoboda K, Kim DS. 2013. Ultrasensitive fluorescent proteins for imaging neuronal activity. *Nature* **499**:295–300.

Dorrn AL, Yuan K, Barker AJ, Schreiner CE, Froemke RC. 2010. Developmental sensory experience balances cortical excitation and inhibition. *Nature* **465**:932–936.

Dubno JR, Eckert MA, Lee FS, Matthews LJ, Schmiedt RA. 2013. Classifying Human Audiometric Phenotypes of Age-Related Hearing Loss from Animal Models. *Jaro-Journal of the Association for Research in Otolaryngology* **14**:687–701. doi:10.1007/s10162-013-0396-x

Eggermont JJ. 2017. Acquired hearing loss and brain plasticity. *Hearing Research* **343**:176–190. doi:10.1016/j.heares.2016.05.008

Ehlers A, Clark DM. 2000. A cognitive model of posttraumatic stress disorder. *Behaviour Research and Therapy* **38**:319–345. doi:10.1016/S0005-7967(99)00123-0

Engineer ND, Riley JR, Seale JD, Vrana WA, Shetake JA, Sudanagunta SP, Borland MS, Kilgard MP. 2011. Reversing pathological neural activity using targeted plasticity. *Nature* **470**:101. doi:10.1038/nature09656

Friedrich J, Zhou P, Paninski L. 2017. Fast online deconvolution of calcium imaging data. *PLoS Comput Biol* **13**:e1005423. doi:10.1371/journal.pcbi.1005423

Garfinkel SN, Liberzon I. 2009. Neurobiology of PTSD: A Review of Neuroimaging Findings. *Psychiatric Annals* **39**. doi:10.3928/00485713-20090527-01

Gerber W, Schoenen J. 1998. Biobehavioral Correlates in Migraine: The Role of Hypersensitivity and Information-Processing Dysfunction. *Cephalalgia* **18**:5–11. doi:10.1177/03331024980018S2103

Gerken GM. 1979. Central denervation hypersensitivity in the auditory system of the cat. *J Acoust Soc Am* **66**:721–727. doi:10.1121/1.383222

Ghanizadeh A. 2011. Sensory Processing Problems in Children with ADHD, a Systematic Review. *Psychiatry Investig* **8**:89. doi:10.4306/pi.2011.8.2.89

Goadsby PJ, Holland PR, Martins-Oliveira M, Hoffmann J, Schankin C, Akerman S. 2017. Pathophysiology of Migraine: A Disorder of Sensory Processing. *Physiological Reviews* **97**:553–622. doi:10.1152/physrev.00034.2015

González-Rodríguez A, Labad J, Seeman MV. 2021. Pain Sensitivity in Schizophrenia Spectrum Disorders: A Narrative Review of Recent Work. *Psychiatry International* **2**:48–58. doi:10.3390/psychiatryint2010004

Grienberger C, Konnerth A. 2012. Imaging Calcium in Neurons. *Neuron* **73**:862–885. doi:10.1016/j.neuron.2012.02.011

Guo W, Hight AE, Chen JX, Klapoetke NC, Hancock KE, Shinn-Cunningham BG, Boyden ES, Lee DJ, Polley DB. 2015. Hearing the light: neural and perceptual encoding of optogenetic stimulation in the central auditory pathway. *Scientific Reports* **5**:10319–10319. doi:10.1038/srep10319

Hannula S, Bloigu R, Majamaa K, Sorri M, Mäki-Torkko E. 2011. Audiogram configurations among older adults: Prevalence and relation to self-reported hearing problems. *International Journal of Audiology* **50**:793–801. doi:10.3109/14992027.2011.593562

Harris JA, Hardie NA, Bermingham-McDonogh O, Rubel EW. 2005. Gene expression differences over a critical period of afferent-dependent neuron survival in the mouse auditory brainstem. *Journal of Comparative Neurology* **493**:460–474. doi:10.1002/cne.20776

Harris JA, Rubel EW. 2006. Afferent regulation of neuron number in the cochlear nucleus: Cellular and molecular analyses of a critical period. *Hearing Research* **216–217**:127–137. doi:10.1016/j.heares.2006.03.016

Hayes SH, Radziwon KE, Stolzberg DJ, Salvi RJ. 2014. Behavioral models of tinnitus and hyperacusis in animals. *Frontiers in neurology* **5**:179–179.

Hebert S, Fournier P, Norena A. 2013. The Auditory Sensitivity is Increased in Tinnitus Ears. *Journal of Neuroscience* **33**:2356–2364. doi:10.1523/JNEUROSCI.3461-12.2013

Heinz MG, Issa JB, Young ED. 2005. Auditory-nerve rate responses are inconsistent with common hypotheses for the neural correlates of loudness recruitment. *Journal of the Association for Research in Otolaryngology* **6**:91–105. doi:10.1007/s10162-004-5043-0

Heinz MG, Young ED. 2004. Response growth with sound level in auditory-nerve fibers after noise-induced hearing loss. *Journal of Neurophysiology* **91**:784–795. doi:10.1152/jn.00776.2003

Herrmann B, Butler BE. 2021a. Aging auditory cortexAssessments, Treatments and Modeling in Aging and Neurological Disease. Elsevier. pp. 183–192. doi:10.1016/B978-0-12-818000-6.00017-2

Herrmann B, Butler BE. 2021b. Hearing loss and brain plasticity: the hyperactivity phenomenon. *Brain Struct Funct* **226**:2019–2039. doi:10.1007/s00429-021-02313-9

Hickox AE, Liberman MC. 2014. Is noise-induced cochlear neuropathy key to the generation of hyperacusis or tinnitus? *Journal of Neurophysiology* **111**:552–564. doi:10.1152/jn.00184.2013

Horwitz AR, Dubno JR, Ahlstrom JB. 2002. Recognition of low-pass-filtered consonants in noise with normal and impaired high-frequency hearing. *The Journal of the Acoustical Society of America* **111**:409–16. doi:10.1121/1.1427357

Issa JB, Haeffele BD, Agarwal A, Bergles DE, Young ED, Yue DT. 2014. Multiscale optical Ca2+ imaging of tonal organization in mouse auditory cortex. *Neuron* 1–16.

Johnson LA, Della Santina CC, Wang X. 2016. Selective Neuronal Activation by Cochlear Implant Stimulation in Auditory Cortex of Awake Primate. *J Neurosci* **36**:12468–12484. doi:10.1523/JNEUROSCI.1699-16.2016

Kamke MR, Brown M, Irvine DRF. 2003. Plasticity in the tonotopic organization of the medial geniculate body in adult cats following restricted unilateral cochlear lesions. *The Journal of Comparative Neurology* **459**:355–367.

Klintwall L, Holm A, Eriksson M, Carlsson LH, Olsson MB, Hedvall Å, Gillberg C, Fernell E. 2011. Sensory abnormalities in autism. *Research in Developmental Disabilities* **32**:795–800. doi:10.1016/j.ridd.2010.10.021

Kotak VC, Fujisawa S, Lee FA, Karthikeyan O, Aoki C, Sanes DH. 2005. Hearing loss raises excitability in the auditory cortex. *The Journal of neuroscience : the official journal of the Society for Neuroscience* **25**:3908–18. doi:10.1523/JNEUROSCI.5169-04.2005

Lewis RM, Jahn KN, Parthasarathy A, Goedicke WB, Polley DB. 2020. Audiometric Predictors of Bothersome Tinnitus in a Large Clinical Cohort of Adults With Sensorineural Hearing Loss. *Otology & Neurotology* **41**:e414–e421. doi:10.1097/MAO.0000000000002568

Li S, Choi V, Tzounopoulos T. 2013. Pathogenic plasticity of Kv7. 2/3 channel activity is essential for the induction of tinnitus. *Proceedings of the National …* **110**:9980–9985. doi:10.1073/pnas.1216671110/-/DCSupplemental.www.pnas.org/cgi/doi/10.1073/pnas.1302770110

Li S, Kalappa BI, Tzounopoulos T. 2015. Noise-induced plasticity of KCNQ2/3 and HCN channels underlies vulnerability and resilience to tinnitus. *eLife* **4**:1–23. doi:10.7554/eLife.0724

Liberman LD, Wang H, Liberman MC. 2011. Opposing gradients of ribbon size and AMPA receptor expression underlie sensitivity differences among cochlear-nerve/hair-cell synapses. *Journal of Neuroscience* **31**:801–808. doi:10.1523/JNEUROSCI.3389-10.2011

Lobarinas E, Salvi R, Ding D. 2013. Insensitivity of the audiogram to carboplatin induced inner hair cell loss in chinchillas. *Hearing research* 1–8.

Luck SJ, Gold JM. 2008. The Construct of Attention in Schizophrenia. *Biological Psychiatry* **64**:34–39. doi:10.1016/j.biopsych.2008.02.014

Manohar S, Spoth J, Radziwon K, Auerbach BD, Salvi R. 2017. Noise-induced hearing loss induces loudness intolerance in a rat Active Sound Avoidance Paradigm (ASAP). *Hearing Research* **353**:197–203. doi:10.1016/j.heares.2017.07.001

Marozeau J, Florentine M. 2007. Loudness growth in individual listeners with hearing losses: A review. *The Journal of the Acoustical Society of America* **122**:EL81–EL87. doi:10.1121/1.2761924

Masri S, Chan N, Marsh T, Zinsmaier A, Schaub D, Zhang L, Wang W, Bao S. 2021. Chemogenetic Activation of Cortical Parvalbumin-Positive Interneurons Reverses Noise-Induced Impairments in Gap Detection. *J Neurosci* **41**:8848–8857. doi:10.1523/JNEUROSCI.2687-19.2021

Müller M, Von Hünerbein K, Hoidis S, Smolders JWT. 2005. A physiological place-frequency map of the cochlea in the CBA/J mouse. *Hearing Research* **202**:63–73. doi:10.1016/j.heares.2004.08.011

Nampiaparampil DE. 2008. Prevalence of Chronic Pain After Traumatic Brain Injury: A Systematic Review. *JAMA* **300**:711. doi:10.1001/jama.300.6.711

Nielsen LA, Henriksson KG. 2007. Pathophysiological mechanisms in chronic musculoskeletal pain (fibromyalgia): the role of central and peripheral sensitization and pain disinhibition. *Best Practice & Research Clinical Rheumatology*, General Musculoskeletal Conditions **21**:465–480. doi:10.1016/j.berh.2007.03.007

Niu Y, Kumaraguru A, Wang R, Sun W. 2013. Hyperexcitability of inferior colliculus neurons caused by acute noise exposure. *Journal of Neuroscience Research* **91**:292–299. doi:10.1002/jnr.23152

Noreña AJ. 2011. An integrative model of tinnitus based on a central gain controlling neural sensitivity. *Neuroscience and Biobehavioral Reviews* **35**:1089–1109. doi:10.1016/j.neubiorev.2010.11.003

Noreña AJ, Moffat G, Blanc JL, Pezard L, Cazals Y. 2010. Neural changes in the auditory cortex of awake guinea pigs after two tinnitus inducers: salicylate and acoustic trauma. *Neuroscience* **166**:1194–1209. doi:10.1016/j.neuroscience.2009.12.063

Norena ArnaudJ, Tomita M, Eggermont JJ. 2003. Neural Changes in Cat Auditory Cortex After a Transient Pure-Tone Trauma. *Journal of Neurophysiology* **90**:2387–2401. doi:10.1152/jn.00139.2003

Nusbaum NJ. 1999. Aging and Sensory Senescence: *Southern Medical Journal* **92**:267–275. doi:10.1097/00007611-199903000-00002

Pachitariu M, Stringer C, Dipoppa M, Schröder S, Rossi LF, Dipoppa M, Rossi LF, Carandini M, Harris KD. 2016. Suite2p : beyond 10 , 000 neurons with standard two-photon microscopy. *bioRxiv* 1–30. doi:10.1101/061507

Parameshwarappa V, Pezard L, Noreña AJ. 2022. Changes in the spatiotemporal pattern of spontaneous activity across a cortical column after noise trauma. *Journal of Neurophysiology* **127**:239–254. doi:10.1152/jn.00262.2021

Parthasarathy A, Hancock KEKE, Bennett K, DeGruttola V, Polley DBDB. 2020a. Bottom-up and top-down neural signatures of disordered multi-talker speech perception in adults with normal hearing. *eLife* **9**. doi:10.7554/eLife.51419

Parthasarathy A, Kujawa SG. 2018. Synaptopathy in the Aging Cochlea: Characterizing Early-Neural Deficits in Auditory Temporal Envelope Processing. *J Neurosci* **38**:7108–7119. doi:10.1523/JNEUROSCI.3240-17.2018

Parthasarathy A, Romero Pinto S, Lewis RM, Goedicke W, Polley DB. 2020b. Data-driven segmentation of audiometric phenotypes across a large clinical cohort. *Scientific Reports* **10**:6704. doi:10.1038/s41598-020-63515-5

Pienkowski M, Tyler RS, Roncancio ER, Jun HJ, Brozoski T, Dauman N, Coelho CB, Andersson G, Keiner AJ, Cacace AT, Martin N, Moore BCJ. 2014a. A Review of Hyperacusis and Future Directions: Part I. Definitions and Manifestations Richard. *American Journal of Audiology* **23**:402–419. doi:10.1044/2014

Pienkowski M, Tyler RS, Roncancio ER, Jun HJ, Brozoski T, Dauman N, Coelho CB, Andersson G, Keiner AJ, Cacace AT, Martin N, Moore BCJ. 2014b. A Review of Hyperacusis and Future Directions: Part II. Measurement, Mechanisms, and Treatment Martin. *American Journal of Audiology* **23**:420–436. doi:10.1044/2014

Pilati N, Ison MJ, Barker M, Mulheran M, Large CH, Forsythe ID, Matthias J, Hamann M. 2012. Mechanisms contributing to central excitability changes during hearing loss. *Proceedings of the National Academy of Sciences of the United States of America* **109**:8292–8297. doi:10.1073/pnas.1116981109

Polley DB, Schiller D. 2022. The promise of low-tech intervention in a high-tech era: Remodeling pathological brain circuits using behavioral reverse engineering. *Neuroscience & Biobehavioral Reviews* **137**:104652. doi:10.1016/j.neubiorev.2022.104652

Popelář J, Syka J, Berndt H. 1987. Effect of noise on auditory evoked responses in awake guina pigs. *Hearing Research* **26**:239–247. doi:10.1016/0378-5955(87)90060-8

Qiu C, Salvi R, Ding D, Burkard R. 2000. Inner hair cell loss leads to enhanced response amplitudes in auditory cortex of unanesthetized chinchillas: evidence for increased system gain. *Hearing Research* **139**:153–171. doi:10.1016/S0378-5955(99)00171-9

Resnik J, Polley DB. 2021. Cochlear neural degeneration disrupts hearing in background noise by increasing auditory cortex internal noise. *Neuron* **109**:984–96. doi:10.1016/j.neuron.2021.01.015

Resnik J, Polley DB. 2017. Fast-spiking GABA circuit dynamics in the auditory cortex predict recovery of sensory processing following peripheral nerve damage. *eLife* **6**. doi:10.7554/eLife.21452

Robertson CE, Baron-Cohen S. 2017. Sensory perception in autism. *Nat Rev Neurosci* **18**:671–684. doi:10.1038/nrn.2017.112

Robertson D, Irvine DRF. 1989. Plasticity of frequency organization in auditory cortex of guinea pigs with partial unilateral deafness. *The Journal of comparative neurology* **282**:456–471. doi:10.1002/cne.902820311

Romero S, Hight AE, Clayton KK, Resnik J, Williamson RS, Hancock KE, Polley DB. 2019. Cellular and widefield imaging of sound frequency organization in primary and higher-order fields of the mouse auditory cortex. *Cerebral Cortex*. doi:10.1101/663021

Sabatini BL. 2019. The impact of reporter kinetics on the interpretation of data gathered with fluorescent reporters (preprint). Neuroscience. doi:10.1101/834895

Sanes DH, Kotak VC. 2011. Developmental plasticity of auditory cortical inhibitory synapses. *Hearing Research* **279**:140–148. doi:10.1016/j.heares.2011.03.015

Sarro EC, Kotak VC, Sanes DH, Aoki C. 2008. Hearing loss alters the subcellular distribution of presynaptic GAD and postsynaptic GABAA receptors in the auditory cortex. *Cerebral Cortex* **18**:2855–2867.

Schecklmann M, Landgrebe M, Langguth B. 2014. Phenotypic characteristics of hyperacusis in tinnitus. *PLoS One* **9**:e86944. doi:10.1371/journal.pone.0086944

Schormans AL, Typlt M, Allman BL. 2018. Adult-onset hearing impairment induces layer-specific cortical reorganization: evidence of crossmodal plasticity and central gain enhancement. *Cerebral Cortex* **29**:1875–1888. doi:10.1093/cercor/bhy067

Schrode KM, Muniak MA, Kim Y-H, Lauer AM. 2018. Central Compensation in Auditory Brainstem after Damaging Noise Exposure. *eNeuro* **5**:ENEURO.0250-18.2018. doi:10.1523/ENEURO.0250-18.2018

Seki S, Eggermont JJ. 2003a. Changes in spontaneous firing rate and neural synchrony in cat primary auditory cortex after localized tone-induced hearing loss. *Hearing Research* **180**:28–38. doi:10.1016/S0378-5955(03)00074-1

Seki S, Eggermont JJ. 2003b. Changes in spontaneous firing rate and neural synchrony in cat primary auditory cortex after localized tone-induced hearing loss. *Hearing Research* **180**:28–38. doi:10.1016/S0378-5955(03)00074-1

Shaheen LA, Liberman MC. 2018. Cochlear synaptopathy changes sound-evoked activity without changing spontaneous discharge in the mouse inferior colliculus. *Frontiers in Systems Neuroscience* **12**:1–19. doi:10.3389/fnsys.2018.00059

Shargorodsky J, Curhan GC, Farwell WR. 2010. Prevalence and Characteristics of Tinnitus among US Adults. *The American Journal of Medicine* **123**:711–718. doi:10.1016/j.amjmed.2010.02.015

Sheintuch L, Rubin A, Brande-Eilat N, Geva N, Sadeh N, Pinchasof O, Ziv Y. 2017. Tracking the Same Neurons across Multiple Days in Ca2+ Imaging Data. *Cell Reports* **21**:1102–1115. doi:10.1016/j.celrep.2017.10.013

Shore SE, Wu C. 2019. Mechanisms of noise-induced tinnitus: insights from cellular studies. *Neuron* **103**:8–20. doi:10.1016/j.neuron.2019.05.008

Strelcyk O, Dau T. 2009. Relations between frequency selectivity, temporal fine-structure processing, and speech reception in impaired hearing. *The Journal of the Acoustical Society of America* **125**:3328–3328. doi:10.1121/1.3097469

Sturm JJ, Zhang-Hooks Y-X, Roos H, Nguyen T, Kandler K. 2017. Noise trauma induced behavioral gap detection deficits correlate with reorganization of excitatory and inhibitory local circuits in the inferior colliculus and are prevented by acoustic enrichment. *The Journal of Neuroscience* **37**:0602–17. doi:10.1523/JNEUROSCI.0602-17.2017

Sun W, Deng A, Jayaram A, Gibson B. 2012. Noise exposure enhances auditory cortex responses related to hyperacusis behavior. *Brain Research* **1485**:108–116. doi:10.1016/j.brainres.2012.02.008

Sun YJ, Wu GK, Liu B, Li P, Zhou M, Xiao Z, Tao HW, Zhang LI. 2011. Fine-tuning of pre-balanced excitation and inhibition during auditory cortical development. *Nature* **465**:927–931.

Syka J, Rybalko N, Popelář J. 1994. Enhancement of the auditory cortex evoked responses in awake guinea pigs after noise exposure. *Hearing Research* **78**:158–168. doi:10.1016/0378-5955(94)90021-3

Tan AYYYY, Atencio CAA, Polley DBB, Merzenich MMM, Schreiner CEE. 2007. Unbalanced synaptic inhibition can create intensity-tuned auditory cortex neurons. *Neuroscience* **146**:449–462. doi:10.1016/j.neuroscience.2007.01.019

Teichert M, Liebmann L, Hübner CA, Bolz J. 2017. Homeostatic plasticity and synaptic scaling in the adult mouse auditory cortex. *Scientific Reports* **7**:17423. doi:10.1038/s41598-017-17711-5

Turrigiano G. 2012. Homeostatic synaptic plasticity: local and global mechanisms for stabilizing neuronal function. *Cold Spring Harbor Perspectives in Biology* **4**:a005736–a005736.

Turrigiano GG. 2008. The Self-Tuning Neuron: Synaptic Scaling of Excitatory Synapses. *Cell* **135**:422–435. doi:10.1016/j.cell.2008.10.008

Vaden KI, Matthews LJ, Eckert MA, Dubno JR. 2017. Longitudinal Changes in Audiometric Phenotypes of Age-Related Hearing Loss. *Jaro-Journal of the Association for Research in Otolaryngology* **18**:371–385. doi:10.1007/s10162-016-0596-2

Wake M, Takeno S, Ibrahim D, Harrison R, Mount R. 1993. Carboplatin ototoxicity: an animal model. *The Journal of laryngology and otology* **107**:585–589. doi:10.1017/S0022215100123771

Wang W, Deng D, Jenkins K, Zinsmaier AK, Zhou Q, Bao S. 2022. Correlation of Electrophysiological and Gene Transcriptional Dysfunctions in Single Cortical Parvalbumin Neurons After Noise Trauma. *Neuroscience* **482**:87–99. doi:10.1016/j.neuroscience.2021.12.006

Wu C, Martel DT, Shore SE. 2016. Increased synchrony and bursting of dorsal cochlear nucleus fusiform cells correlate with tinnitus. *Journal of Neuroscience* **36**:2068–2073.

Wu GK, Li P, Tao HW, Zhang LI. 2006. Nonmonotonic synaptic excitation and imbalanced inhibition underlying cortical intensity tuning. *Neuron* **52**:705–715.

Yang S, Su W, Bao S. 2012. Long-term, but not transient, threshold shifts alter the morphology and increase the excitability of cortical pyramidal neurons. *Journal of neurophysiology* **108**:1567–1574. doi:10.1152/jn.00371.2012

Yang S., Weiner BD, Zhang LS, Cho S-J, Bao S. 2011. Homeostatic plasticity drives tinnitus perception in an animal model. *Proceedings of the National Academy of Sciences* **108**:14974–14979. doi:10.1073/pnas.1107998108

Yang Sungchil, Weiner BD, Zhang LS, Cho S-JS-J, Bao S. 2011. Homeostatic plasticity drives tinnitus perception in an animal model. *Proceedings of the National Academy of Sciences* **108**:14974–14979. doi:10.1073/pnas.1107998108

Yunus MB. 2007. Fibromyalgia and Overlapping Disorders: The Unifying Concept of Central Sensitivity Syndromes. *Seminars in Arthritis and Rheumatism* **36**:339–356. doi:10.1016/j.semarthrit.2006.12.009

Zeng FG. 2020. Tinnitus and hyperacusis: central noise, gain and variance. *Current Opinion in Physiology* **18**:123–129. doi:10.1016/j.cophys.2020.10.009

Zeng FG. 2013. An active loudness model suggesting tinnitus as increased central noise and hyperacusis as increased nonlinear gain. *Hearing Research* **295**:172–179. doi:10.1016/j.heares.2012.05.009

FIGURES & LEGENDS

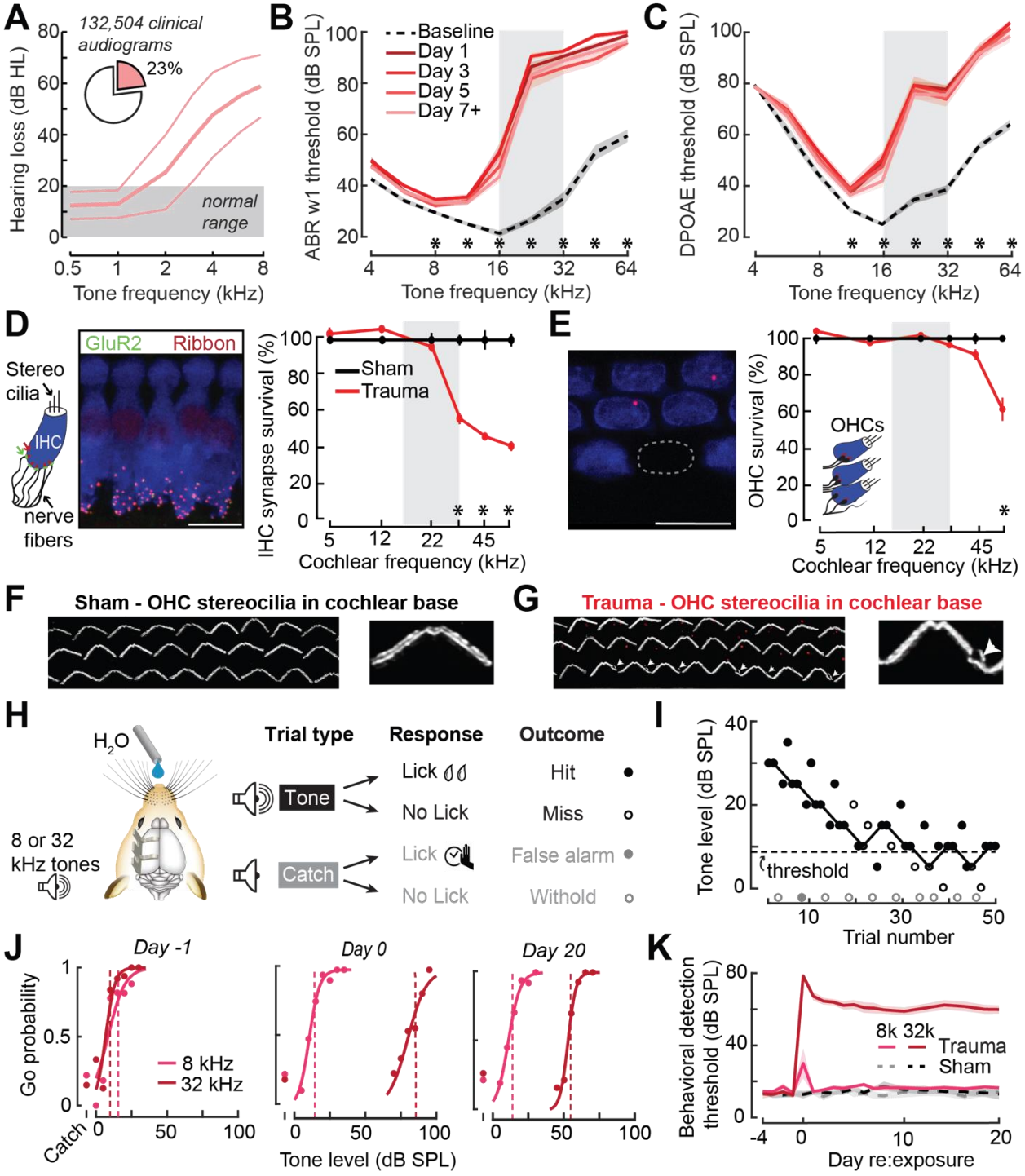

FIGURE 1. Electrophysiological, anatomical, and behavioral confirmation of noise-induced, high-frequency sensorineural hearing loss.

(A) In human subjects, analysis of 132,504 pure tone audiograms indicate that 23% of visitors to our audiology clinic present with steeply sloping high-frequency hearing loss. Values represent mean ± SD hearing thresholds in units of dB hearing loss (HL).

(B-C) In mice, response thresholds for wave 1 of the auditory brainstem response (ABR, *B*) and cochlear DPOAE (*C*) measured before and at various timepoints after acoustic trauma show a permanent threshold shift at high frequencies (2-way repeated measures ANOVAs, Frequency × Time interaction terms for ABR wave 1 [$F = 87.51$, $p = 6 \times 10^{-26}$] and DPOAE [$F = 46.44$, $p = 2 \times 10^{-29}$]). Asterisks denote significant differences between baseline and Day 7+ measurements with post-hoc pairwise comparisons ($p < 0.05$).

(D) Cochlea immunostained for anti-CtBP2 and anti-GluR2a reveal reduced presynaptic ribbon and post-synaptic glutamate receptor patches, respectively, at high-frequency regions of the cochlea (>22 kHz) in trauma mice compared to sham exposure controls (Mixed model ANOVA with Group as a factor, Frequency as a repeated measure, and cochlear synapse count as the outcome measure: Group × Frequency interaction term, $F = 22.33$, $p = 4 \times 10^{-11}$). Asterisks denote significant differences between Sham and Trauma with post-hoc pairwise comparisons ($p < 0.05$).
(E) Loss of outer hair cell (OHC) bodies is limited to the extreme basal regions of the cochlea in noise-exposed animals (Group × Frequency interaction term, $F = 11.54$, $p = 4 \times 10^{-7}$).
(F-G) Anatomical substrates for cochlear threshold shifts (*B and C)* in more apical cochlear regions can be linked to comparatively subtle OHC stereocilia damage, as visualized by anti-Espin immunolabeling of actin bundle proteins. Cochlear location is approximately 32 kHz. Scale bars represent 10 μm.
(H) Schematic depicts the design of a head-fixed Go/NoGo tone detection task.
(I) A modified 2-up, 1-down adaptive staircasing approach to study tone detection thresholds. Example data shows one run of 8 kHz tone detection, which finishes at 6 reversals.
(J) Logistical fits of 8- and 32-kHz Go probability functions for one mouse measured before, hours after, and 20 days following acoustic trauma. Dotted lines show threshold as determined by the adaptive tracking method.
(K) Daily behavioral threshold measurements from 13 mice (N = 7 trauma) over an approximate 3-week time period shows a permanent increase in 32 kHz threshold but not 8 kHz after acoustic trauma (Mixed model ANOVA with Group as a factor and both Frequency and Time as repeated measures, main effects for Group [$F = 157.76$, $p = 8 \times 10^{-8}$], Frequency [$F = 368.87$, $p = 9 \times 10^{-10}$], and Time [$F = 44.21$, $p = 6 \times 10^{-53}$], Group × Frequency × Time interaction [$F = 37.98$, $p = 2 \times 10^{-48}$].

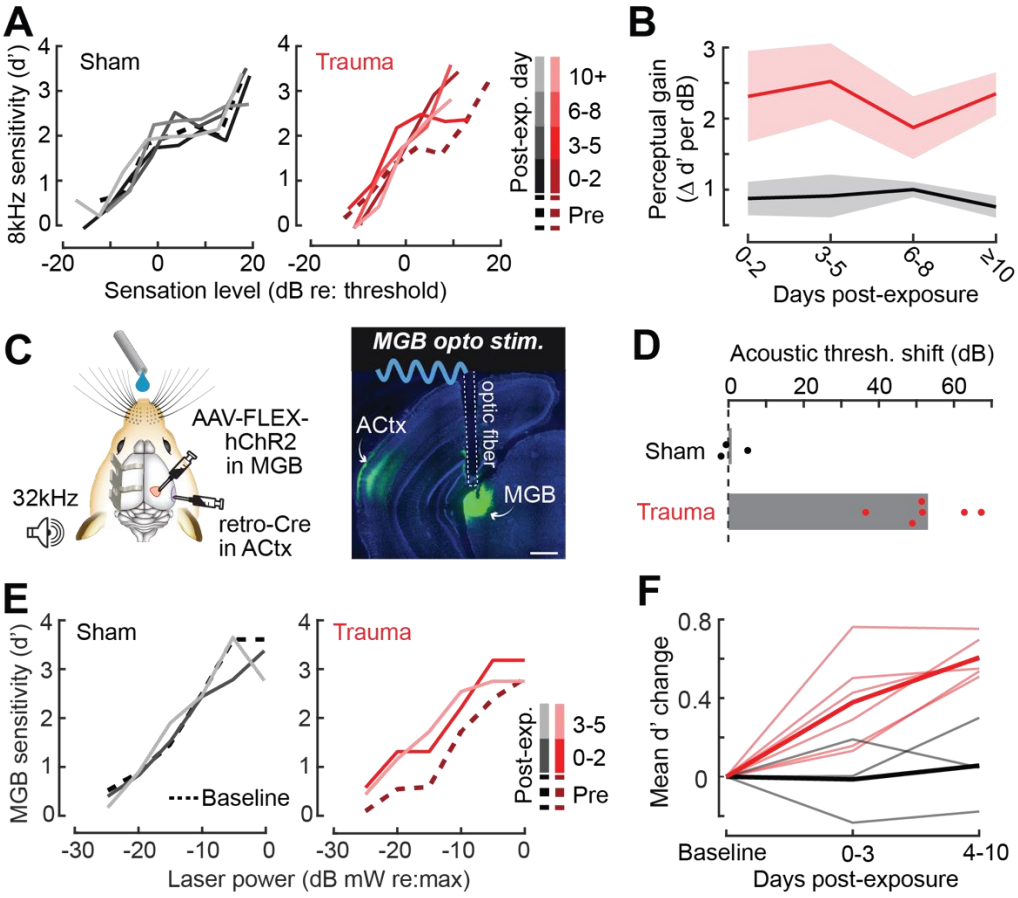

FIGURE 2. Hypersensitivity to sound and direct auditory thalamocortical stimulation following acoustic trauma.

(A) Behavioral detection functions (reported as the sensitivity index, d') across time for sham- and noise-exposed example mice show hypersensitivity to spared, low-frequency tones.

(B) Change in perceptual gain for the 8 kHz tone, measured as the mean increase in d' per dB increase in sound level, relative to baseline performance. Perceptual gain for an 8kHz tone is increased in acoustic trauma mice (N = 7) compared to sham (N = 6) but does not change over post-exposure time (ANOVA with Group as a factor and Time as a repeated measure, main effect for Group, $F = 12.42$, $p = 0.005$; main effect for Time, $F = 0.52$, $p = 0.67$).

(C) *Left,* Preparation for the mixed modality optogenetic and tone detection task. *Right,* ChR2 expression in auditory thalamocortical neurons and placement of the implanted optic fiber relative to retrogradely labeled cell bodies in the medial geniculate body (MGB).

(D) During 32kHz tone detection blocks, detection thresholds are elevated by approximately 50 dB following trauma (N=6, paired t-test, $p = 0.0001$) but no change was noted in sham-exposed mice (N=3, $p = 0.74$).

(E) Psychometric detection functions for optogenetic auditory thalamocortical stimulation before and after acoustic trauma or sham exposure in two example mice.

(F) Summed change across the d' function relative to baseline, for noise- and sham-exposed mice. Individual mice thin lines, group mean thick lines. After trauma, mice became hypersensitive to MGB stimulation, suggesting an auditory thalamocortical contribution to perceptual hypersensitivity (ANOVA with Group as a factor and post-exposure Time as a repeated measure; main effect for Group, $F = 15.54$, $p = 0.006$; main effect for time, $F = 4.65$, $p = 0.07$).

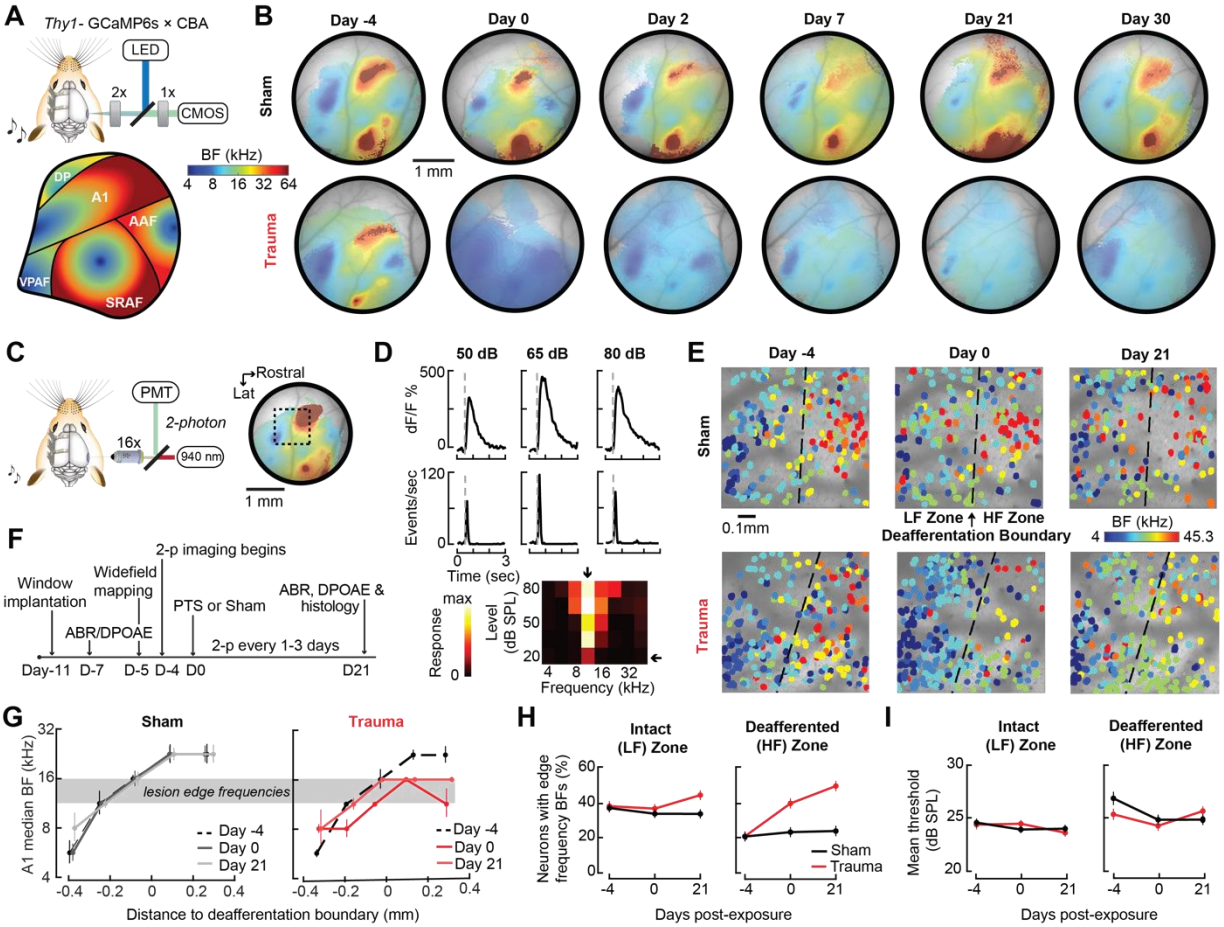

FIGURE 3. Tonotopic remapping within the cortical deafferentation zone revealed by chronic mesoscale and cellular calcium imaging

(A) *Top,* Approach for widefield calcium imaging using a tandem lens epifluorescence microscope in awake Thy1-GCaMP6s x CBA/CaJ mice that express GCaMP6s in pyramidal neurons (PyrNs). *Bottom*, Schematic depicts the typical arrangement of individual fields within the ACtx based on tonotopic BF gradients (as detailed in Romero et al., 2019).

(B) Chronic widefield best frequency (BF) maps in example sham and trauma mice (top and bottom, respectively) shows BF remapping within the deafferented high-frequency regions throughout the ACtx after acoustic trauma.

(C) *Left,* approach for chronic 2-photon calcium imaging of layer 2/3 PyrN's along the A1 tonotopic gradient. *Right,* 2-photon imaging field of view superimposed on the widefield BF map measured in another example mouse.

(D) *Top,* Example of tone-evoked GCaMP transients measured as the fractional change in fluorescence and deconvolved activity. *Bottom,* Peak deconvolved amplitudes for tones of varying frequencies and levels are used to populate the complete frequency-response area and derive the BF (downward arrow) and threshold (leftward arrow) for each neuron.

(E) BF arrangements in L2/3 PyrNs measured at three times over the course of a month in representative sham and trauma mice. A support vector machine (SVM) was trained to bisect the low- and high-frequency zones of the A1 BF map (LF [< 16 kHz] and HF [≥ 16 kHz], respectively). The dashed line represents the SVM-derived boundary to segregate the LF and HF. The SVM line is determined for each mouse on Day -4 and then applied to the same physical location for all future imaging sessions following alignment.

(F) Timeline for chronic 2-photon imaging and cochlear function testing in each sham and trauma mouse.

(G) Individual PyrNs are placed into five distance categories based on their Euclidean distance to the SVM line and the BF of each category is expressed as the median ± bootstrapped error. Following trauma, BFs in the HF zone are remapped to sound frequencies at the edge of the cochlear lesion.

(H) Across all tone-responsive PyrNs measured at three time points, the percent of neurons with BFs corresponding to edge frequencies (11.3-16kHz) was greater in trauma mice (N = 4 mice, n = 1749 PyrNs)

than sham (N = 4 mice, n = 1748 PyrNs), was greater in the deafferented HF region than the intact LF region, and increased over time in trauma mice compared to sham controls (3-way ANOVA with Group, Region, and Time as factors: main effect for Group, $F = 34.29$, $p = 5 \times 10^{-9}$; Group × Region interaction term, $F = 7.42$, $p = 0.007$; Group × Time interaction term, $F = 10.17$, $p = 0.00004$).

(I) Competitive expansion of edge frequency BFs in the deafferented HF zone was not accompanied by a change in neural response threshold (3-way ANOVA: main effect for Group, $F = 0.8$, $p = 0.37$; Group × Region interaction term, $F = 0.93$, $p = 0.33$; Group × Time interaction term, $F = 1.33$, $p = 0.27$).

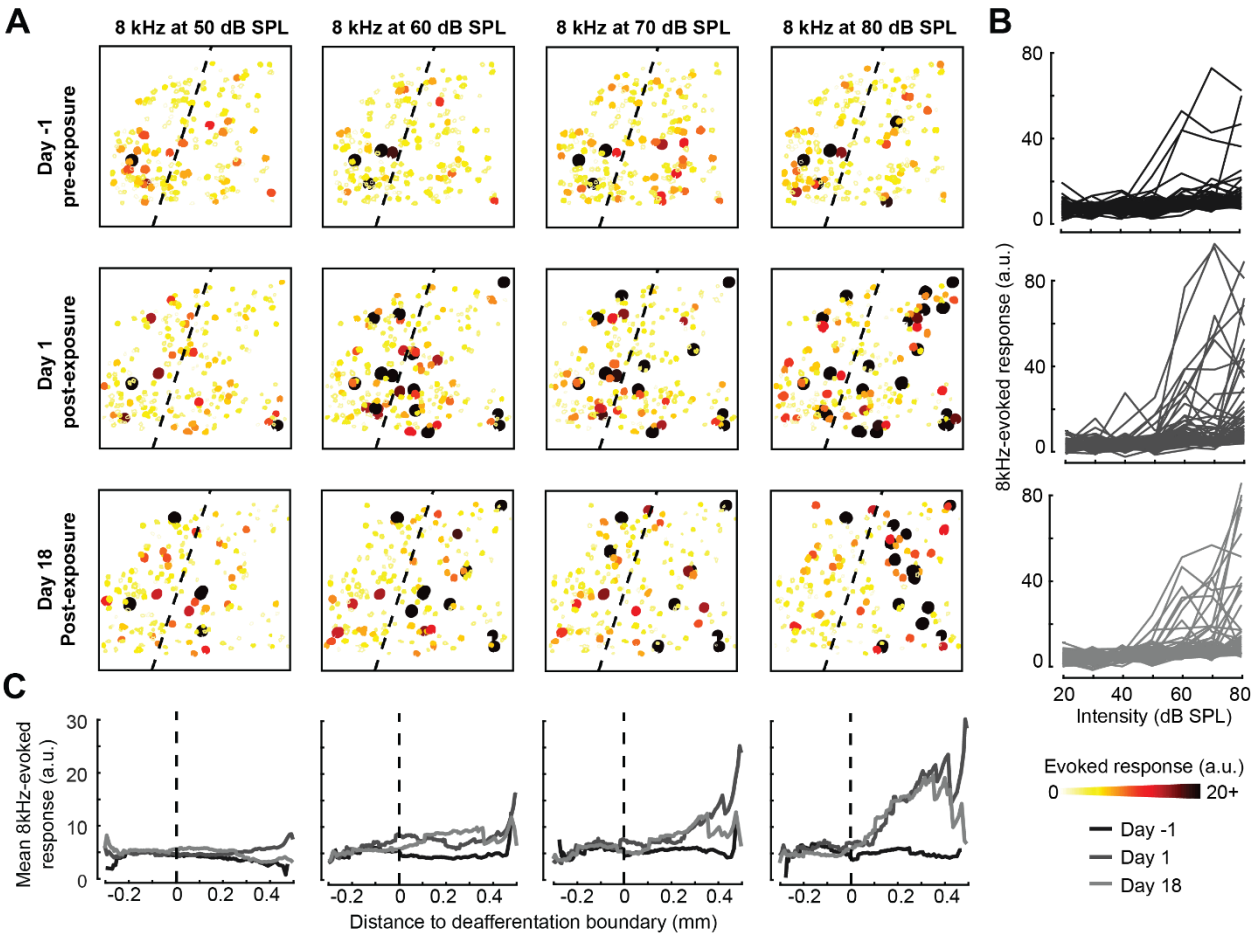

FIGURE 4. Spatial and temporal expression of excess central gain following acoustic trauma.
(A) Response amplitudes to 8 kHz tones presented at varying levels (columns) and days (rows) relative to noise exposure for 185 PyrNs in an example mouse.
(B) Intensity-response functions for 66 randomly selected PyrNs recorded on days -4, 1, and 18 relative to the day of noise exposure.
(C) Mean tone-evoked responses for all PyrNs relative to the SVM deafferentation boundary at 50-80 dB SPL plotted separately for each of the three days.

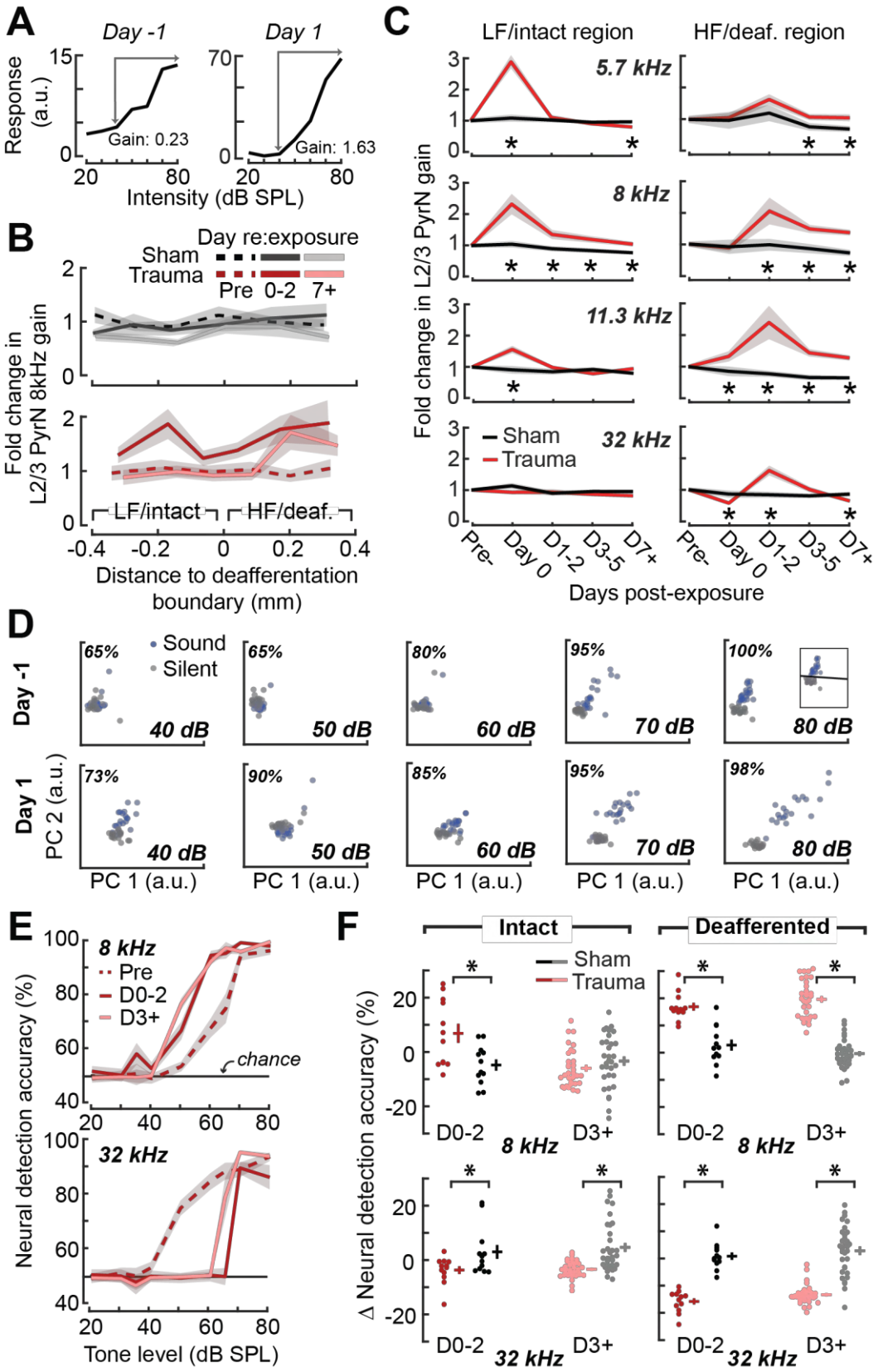

FIGURE 5. Increased central gain is associated with hypersensitive neural encoding of low-intensity sounds.

(A) Neural gain is measured as the average rate of response growth in the sound level-response function. A detailed description of how neural gain is measured for different types of level-response functions is provided in **Figure 5 – Figure supplement 1**.

(B) Mean change in response gain to an 8 kHz tone relative to the baseline SVM demarcation of the low-frequency (LF) intact and high-frequency (HF) deafferented regions of the A1 map from all sham-exposed (*top*) and all noise-exposed (*bottom*) mice.
(C) Fold change in 8 kHz response gain relative to the pre-exposure period in sham (n = 23,007 PyrNs from 4 mice) and trauma (n = 23,319 PyrNs from 4 mice). After acoustic trauma, the response gain for low-frequency tones is temporarily increased in the intact region. A sustained increase in response gain is observed in the deafferented region, particularly for tone frequencies bordering the cochlear lesion. Four-way ANOVA with Group, Region, Time, and Frequency as factors (main effects, respectively: $F = 111.03$, $p = 6\times10^{-26}$; $F = 0.03$, $p = 0.87$; $F = 23.21$, $p = 4\times10^{-19}$; $F = 9.87$, $p = 2\times10^{-6}$; Group × Region × Time × Frequency interaction term: $F=2.23$; $p = 0.008$. Asterisks denote significant pairwise post-hoc differences between groups ($p < 0.05$).
(D) Neural ensemble responses to single trials of sound or silence were decomposed into principal components (PC) and classified with an SVM decoder. The first two PCs are presented from an example mouse 1 day before or after acoustic trauma for an 8 kHz tone. Single trial classification accuracy is provided for each sound intensity.
(E) Mean decoding accuracy for 8 and 32 kHz tones across all noise-exposed mice as a function of sound intensity at varying times following acoustic trauma.
(F) Mean change in decoding accuracy across all intensities for 8 and 32 kHz tones for L2/3 PyrNs in the intact and deafferented regions of the A1 map. For 8 kHz tones, PyrN ensemble decoding shows sustained improvement in the deafferented region but a temporary improvement in the intact region. Ensemble decoding of 32 kHz tones is reduced for all time points and measurement regions. Dots represent single imaging sessions. Bars denote mean ± SEM. Asterisks represent significant differences with unpaired t-tests ($p < 0.05$).

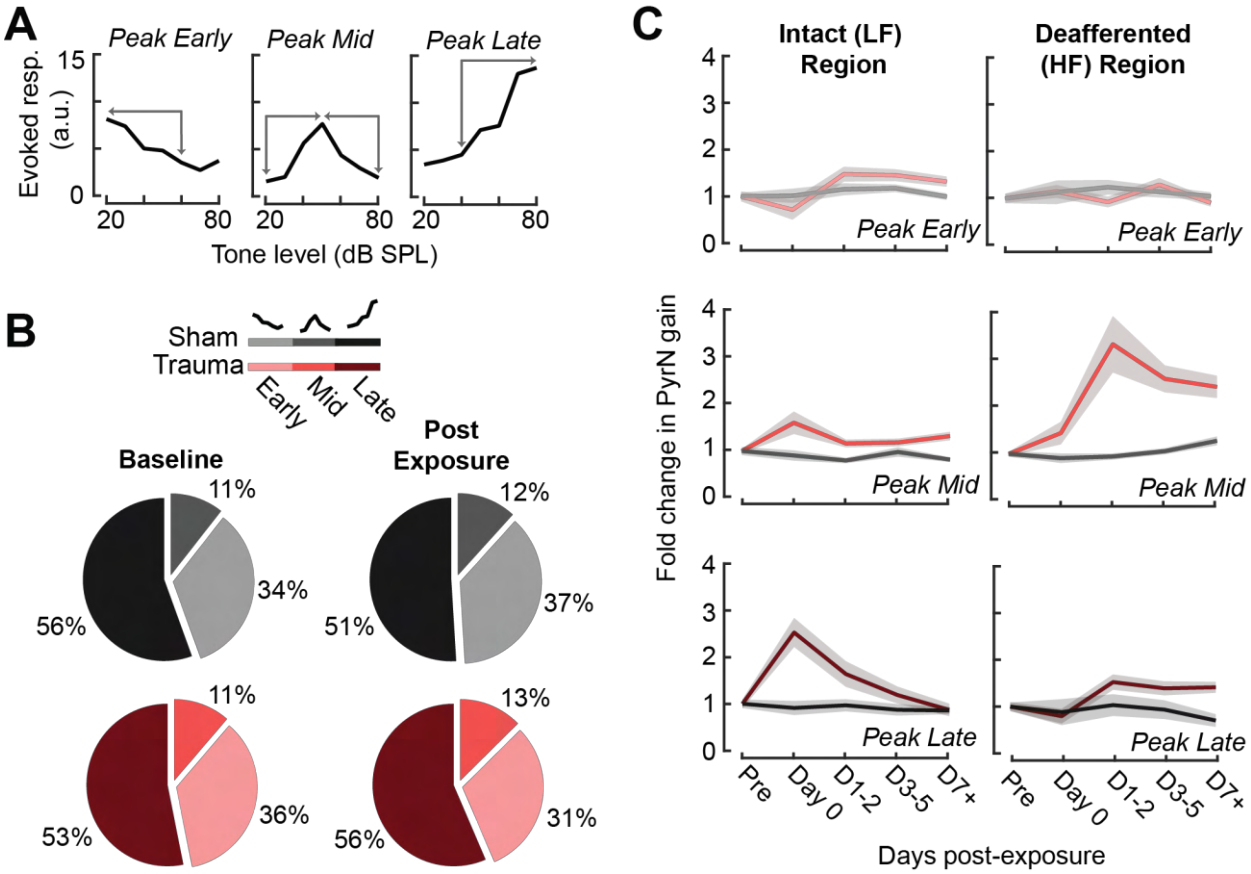

Figure 5 – figure supplement 1. Assessment of gain measurement for different intensity-response function shapes.

(A) Tone-responsive neurons were assigned to one of three categories depending on the location of the intensity-response function peak (i.e., the best level). The gain was calculated as the absolute change in response over the intensity range(s) indicated by the arrows.

(B) The prevalence of the different function shapes for both noise- and sham-exposed mice at baseline and post-exposure D1-3.

(C) Rather than collapsing gain changes across response function types (as per **Figure 5C**), analyzing each response type individually reveals that excess central gain is not observed in Peak Early types and is expressed most strongly in the Peak Mid intensity response growth functions.

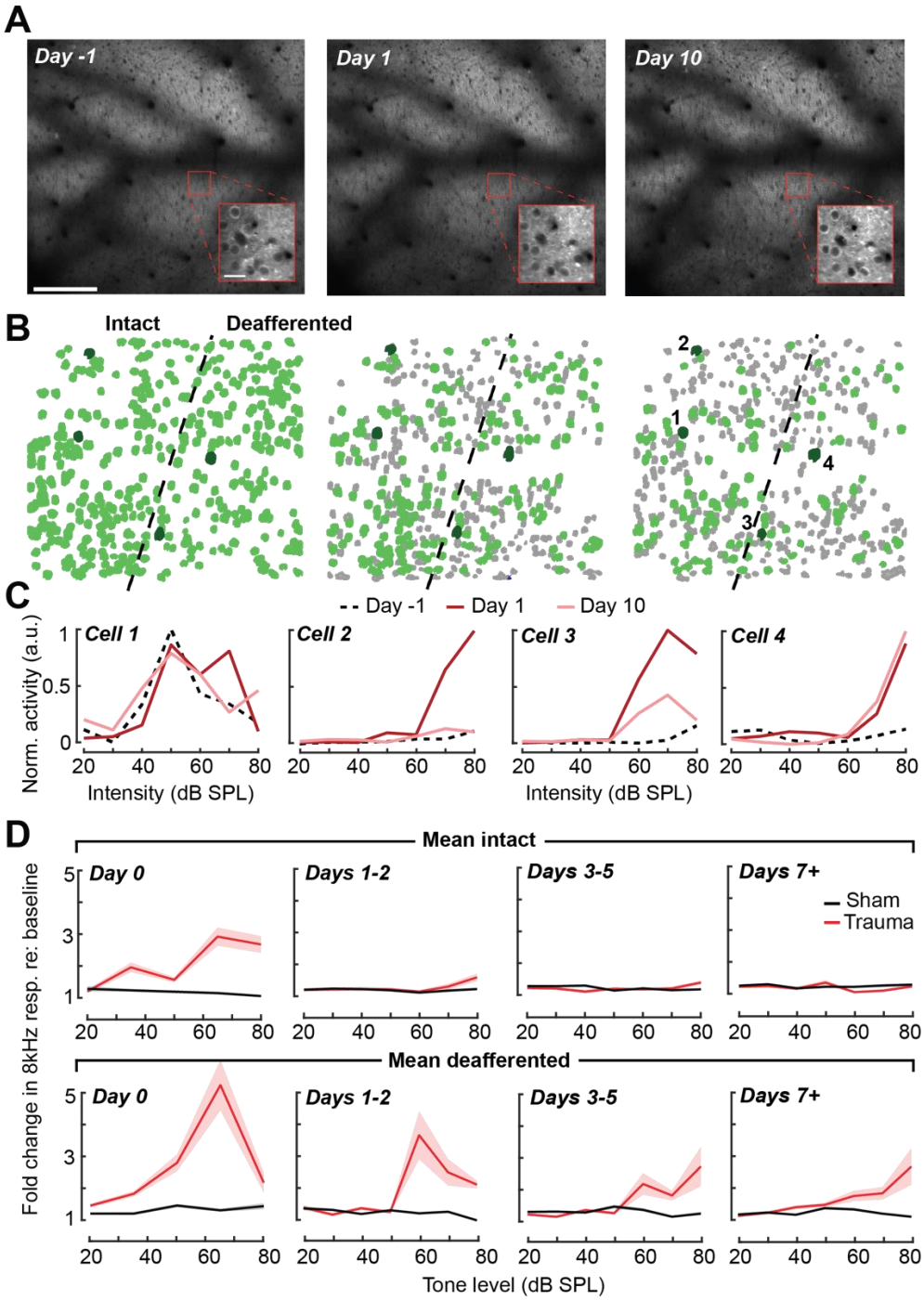

FIGURE 6. Tracking single neuron response gain dynamics over a several week period before and after noise exposure.

(A) Example fields-of-view from a single mouse showing the same imaging field over a several week period. Insets show data acquired at 4× digital zoom. Scale bar is 200 μm, inset scale bar is 20 μm.

(B) Single L2/3 PyrN ROI masks. Green masks indicate cells found on the current day and all previous days using a cell score threshold of 0.8 (see **Figure 6 – Figure supplement 1**).

(C) Normalized 8 kHz intensity-response functions for the four PyrNs highlighted in *B*. Neurons in the intact region show temporary increases in their responses while neurons in the deafferented region show permanent hyperresponsiveness.

(D) Mean fold change in response to 8 kHz tones of varying intensities for individual neurons relative to their own response function measured prior to noise exposure (n = 303/552, trauma/sham). Gain is strongly elevated in both regions hours after trauma. Sustained gain increases are observed in the deafferented zone for at least one week following trauma but not in the intact zone. Four-way ANOVA with Group and Region as factors, and Time and Intensity as repeated measures (main effects, respectively: F = 6.87, p =

0.01; F = 2.9, p = 0.09; F = 8.69, p = 4×10^{-5}; F = 116.61, p = 8×10^{-13}; Group × Region × Time × Intensity interaction term: F=6.65; p = 0.0004).

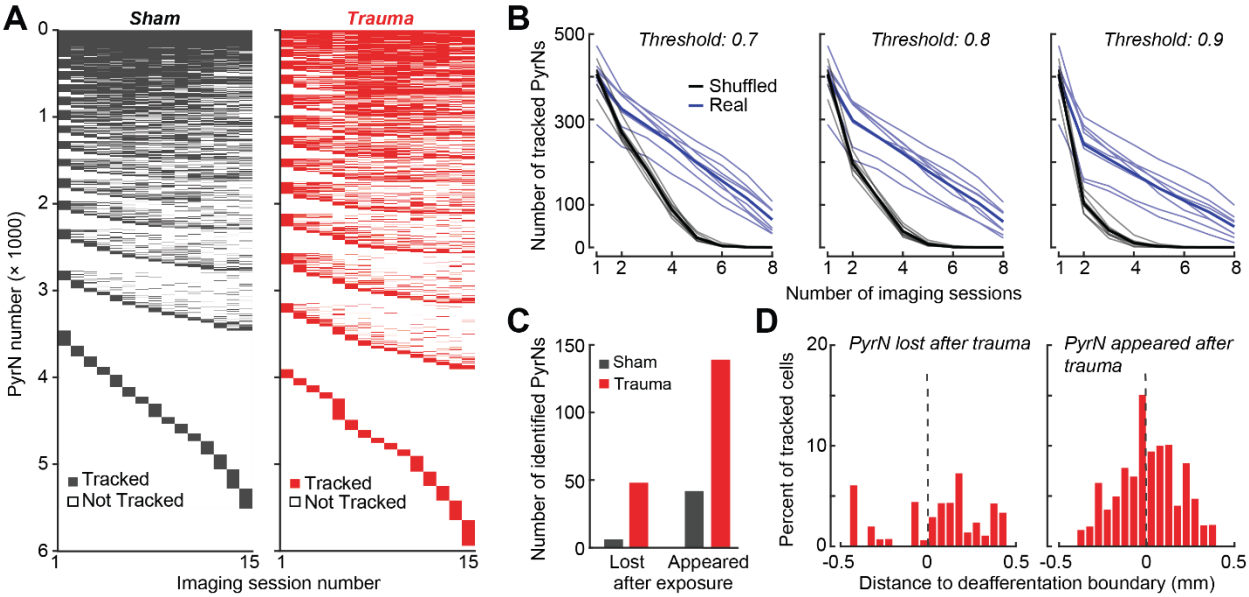

Figure 6 – Figure supplement 1. Validation of single cell tracking over imaging days.
(A) Representation of all neurons found across noise- and sham-exposed mice. Cells are initially sorted by both the number of sessions they were tracked (descending order) and then by the first session they were identified (ascending order).
(B) To set criteria for identifying chronically tracked cells, we performed the same tracking algorithm on shuffled fields-of-view taken from the eight different mice. We've plotted the number cells tracked across 8 sessions in real and shuffled data sets for different confidence thresholds. Falsely tracked PyrNs were not observed at a confidence threshold of 0.8 at 8 sessions
(C) Cells reliably tracked for multiple baseline sessions that disappeared after noise exposure were labeled 'lost', while cells not present at baseline that were subsequently identified and tracked for many sessions after noise exposure were labelled 'appeared'.
(D) After trauma, the location of the 'lost' and 'appeared' cells in the cortical map relative to the total number of cells found at each location and expressed as a percentage. Lost cells were largely found in the deafferented (high frequency) region, while appeared cells were concentrated around the deafferentation boundary.

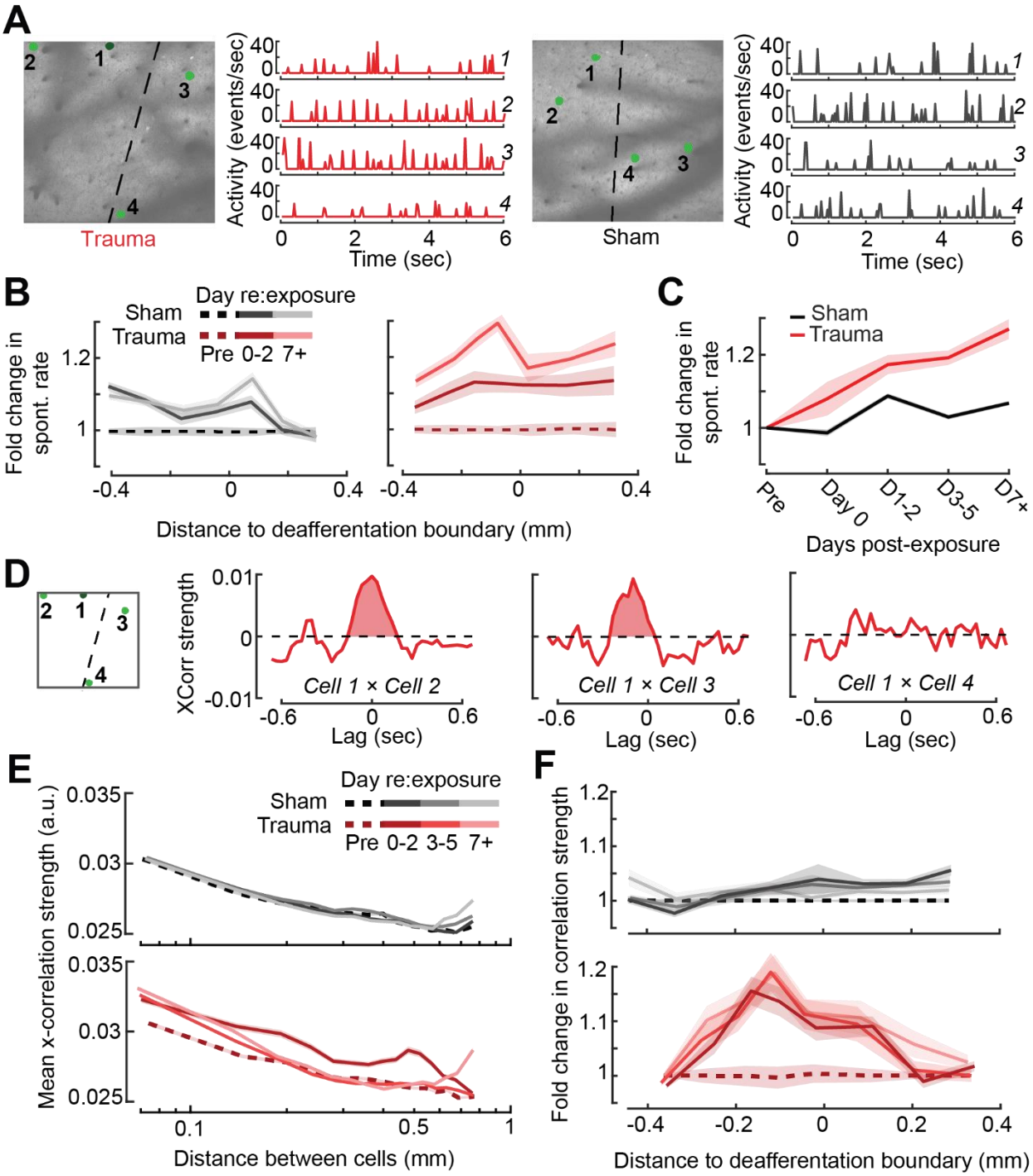

FIGURE 7. Topographic regulation of neural hyperexcitability and hyper-synchrony after acoustic trauma.

(A) Spontaneous activity traces in four example neurons from a trauma (*left*) and sham (*right*) mouse.

(B) In chronically tracked PyrNs, spontaneous activity changes are expressed as fold change relative to that cell's pre-exposure baseline. Increased spontaneous activity after trauma (*right*) or the lack thereof after sham exposure (*left*) are plotted over topographic distance and over post-exposure time.

(C) Spontaneous activity changes across the cortical map are significantly greater after trauma than sham exposure and increase over post-exposure time (n = 915/1125 tracked cells, for trauma/sham; Mixed model ANOVA with Group as a factor and Time as a repeated measure, main effect for Group [$F = 12.81$, $p = 0.0004$], main effect for Time [$F = 65.03$, $p = 3 \times 10^{-40}$], Group × Time interaction term [$F = 17.66$, $p = 3 \times 10^{-11}$]).

(D) Synchrony in the spontaneous activity of PyrN pairs is measured as the area under the shuffle-corrected cross-correlogram peak (shaded red region, see **Methods**). Example data are plotted for the same four PyrNs with topographic positions indicated in left panel.
(E) Looking across all significantly correlated PyrN pairs recorded in a given imaging session (n = 3,301,363 pairs, 1,624,195/1,677,168 for trauma/sham), neural synchrony is reduced as the physical separation between somatic ROIs increases. Synchrony is increased after trauma, though remains elevated only among nearby PyrNs (3-way ANOVA with Group, Day, and Distance as factors: main effects for Group [$F = 556.94$, $p = 4 \times 10^{-123}$], Day [$F = 82.6$, $p = 2 \times 10^{-53}$], and Distance [$F = 8527.73$, $p = 0$], Group × Day × Distance interaction term [$F = 7.94$, $p = 3 \times 10^{-5}$]).
(F) For each chronically tracked neuron (same sample as *C*), we calculate their average neural synchrony with all other cells (only taking significant pairs). Given the location of these tracked cells, we can examine the fold change in neural synchrony relative to pre-exposure baseline across the topographic map. Neural synchrony is significantly and stably increased after trauma, particularly for PyrNs located near the deafferentation boundary (Mixed model ANOVA with Group and Distance as factors and Day as a repeated measure: main effects for Group [$F = 26.62$, $p = 3 \times 10^{-7}$], Day [$F = 1.68$, $p = 0.19$], and Distance [$F = 0.53$, $p = 0.47$], Group × Distance interaction term [$F = 5.53$, $p = 0.02$]).

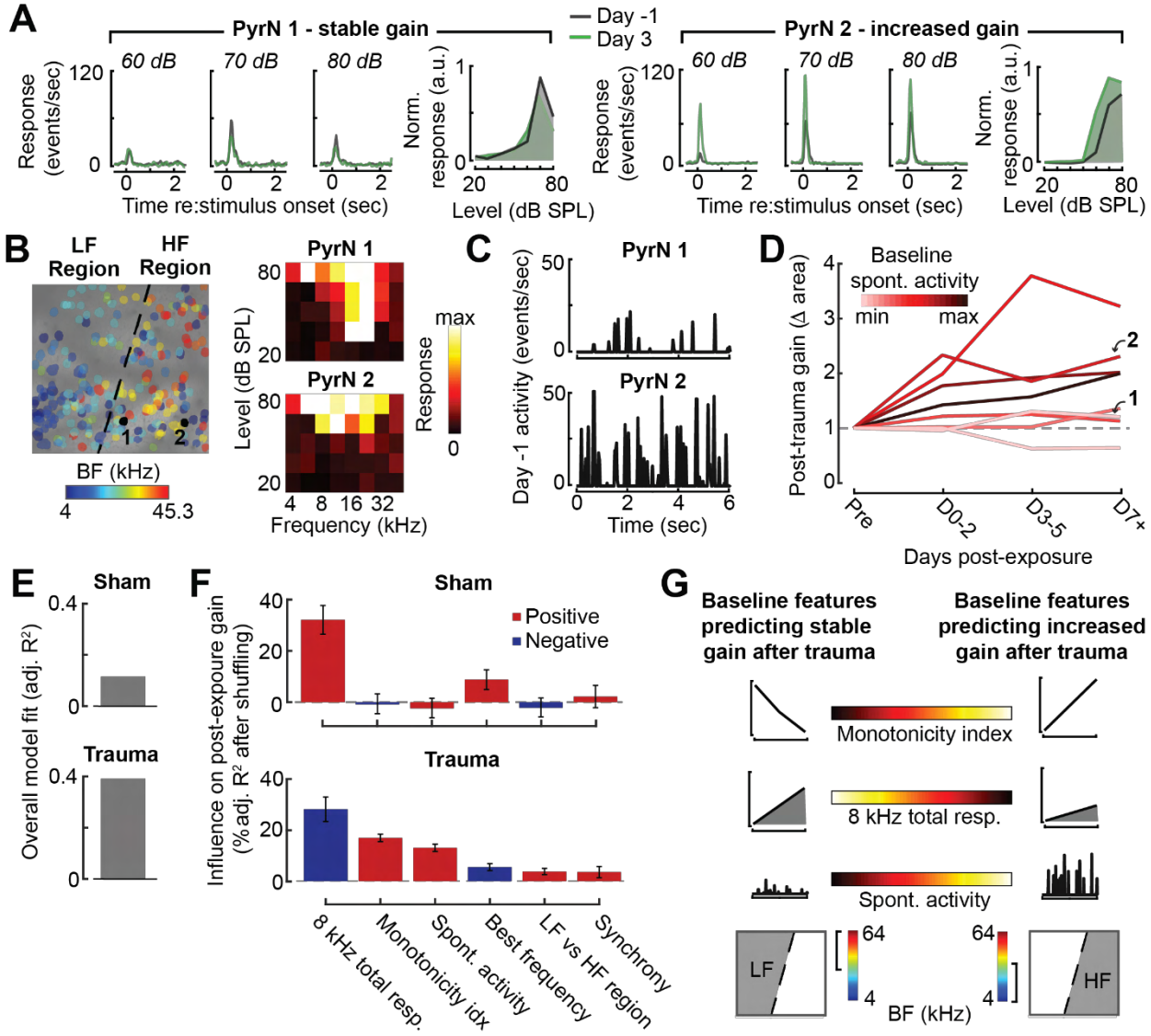

FIGURE 8. Identifying baseline features in single PyrNs that predict stable versus excess gain changes after acoustic trauma.

(A) Two exemplar tracked neurons illustrating stable (*left*) and excess (*right*) response growth to an 8 kHz tone following acoustic trauma.

(B) Both neurons are located in the deafferented map region but had different BFs and frequency tuning properties measured during the baseline imaging session.

(C) Spontaneous activity for the same two PyrNs also differed at baseline.

(D) For tracked neurons, gain is measured as the fold change in the area under the intensity-response growth function relative to the pre-exposure baseline (see **Figure 8 – figure supplement 1A**). In 8 representative neurons, a higher spontaneous activity rate at baseline was associated with excess central gain after trauma. Arrows denote PyrNs 1 and 2 shown in *A-C.*

(E) A linear model used various pre-exposure properties of chronically tracked neurons to predict their change in gain (see **Methods**). Models were fit separately for PyrNs recorded from trauma (n = 510) and sham (n = 749) mice.

(F) For each model, individual predictor variables were shuffled and the models were re-fit. The resulting decrease in the adjusted r-squared is shown for variables in both models, and bars are color-coded by the sign of the relationship of each predictor variable with the response variable. Errors are bootstrapped. For the full model see **Figure 8 – figure supplement 1B**. Predictor variables in order: area under the baseline 8 kHz intensity-response growth function, monotonicity index for the 8 kHz intensity-response function defined as the response at the maximum intensity divided by the response at the best intensity, mean spontaneous

activity, BF, an indicator variable for whether the cell is in the deafferented or intact region, and the strength of correlated activity between the PyrN and its neighbors.
(G) A graphical summary of the linear model results schematize the baseline factors most strongly associated with stable (*left*) or excess (*right*) gain after trauma.

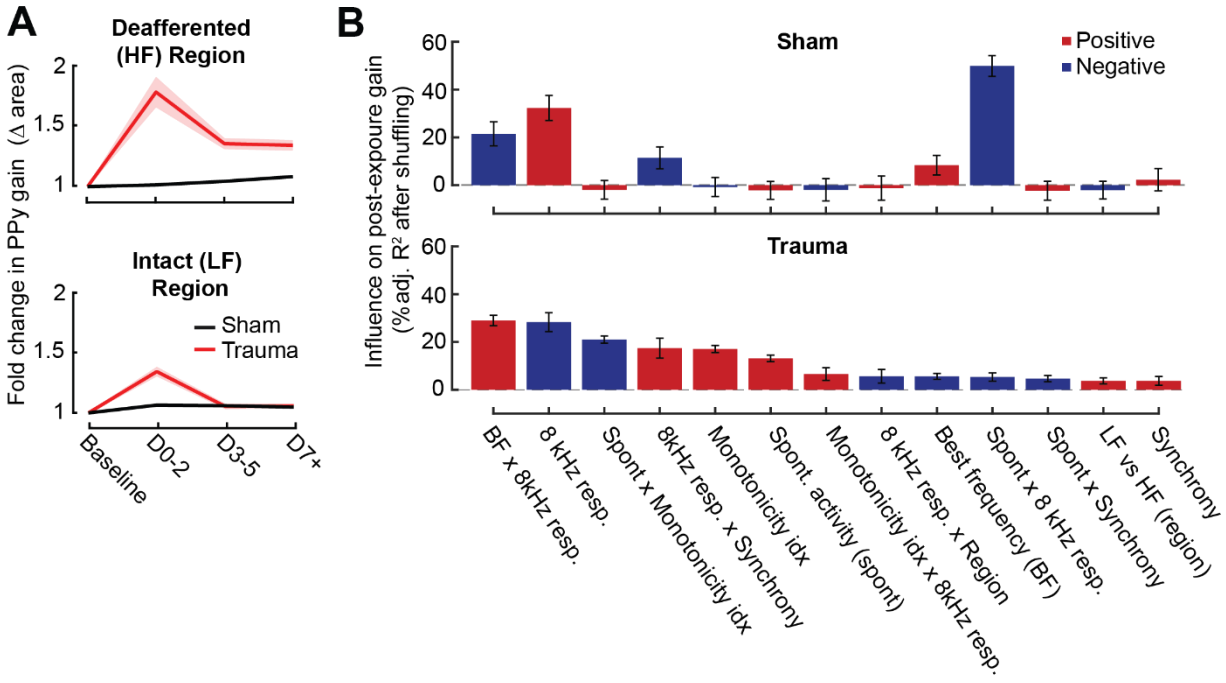

Figure 8 – figure supplement 1. Extended description of the multi-variate linear model analysis in sham and trauma mice.
(A) For tracked neurons, gain for an 8 kHz tone was measured as the area under the intensity-response function relative to the baseline area. Neurons in the intact region show a temporary increase in gain after trauma, while neurons in the deafferented region show permanent changes in gain. The fold change in area is the response variable for the linear model.
(B) For each model, individual predictor variables were shuffled and the models were re-fit. The resulting decrease in the adjusted r-squared is shown for variables in both models, and bars are color-coded by the sign of the relationship of each predictor variable with the response variable. Errors are bootstrapped.

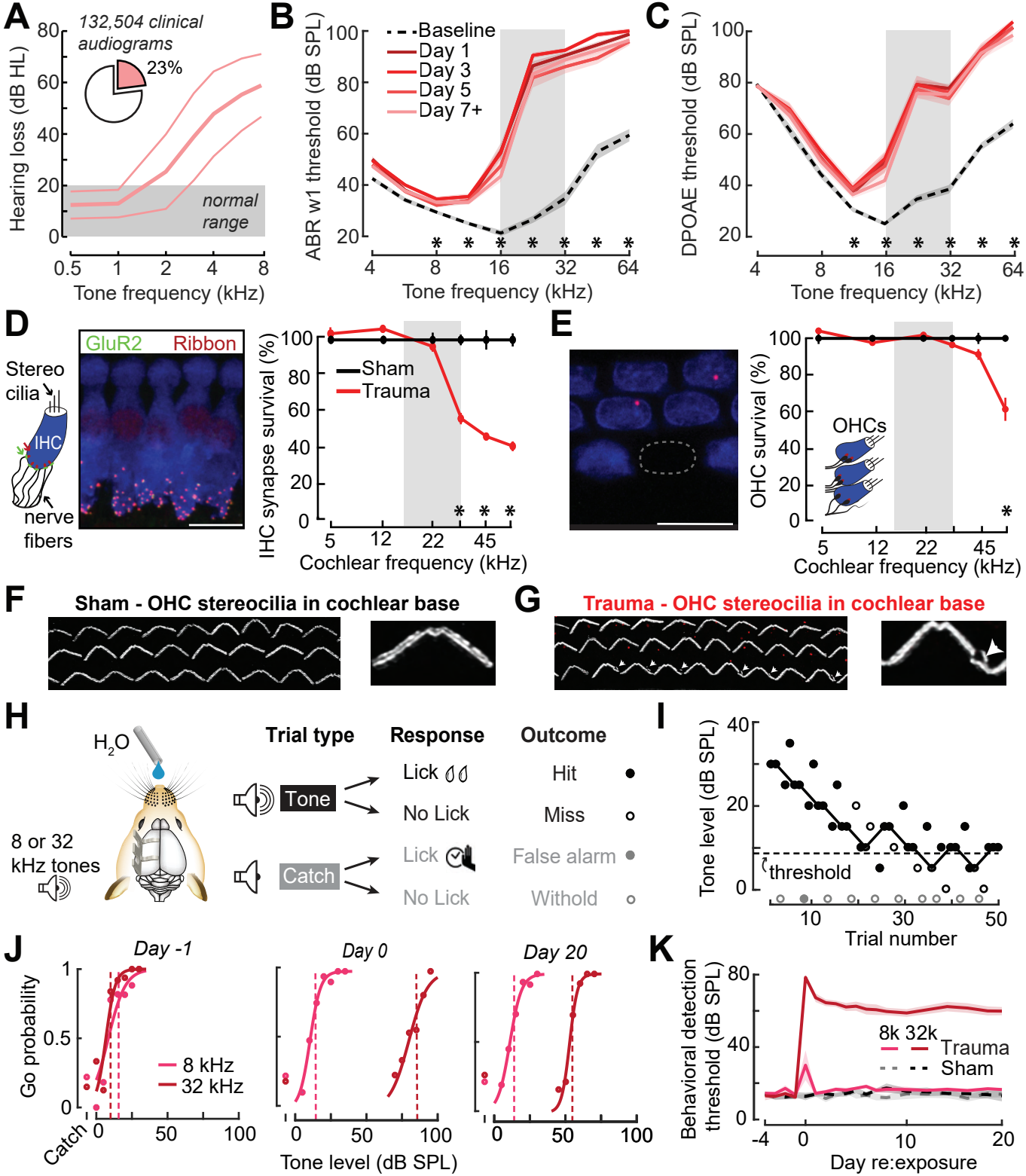
A
132,504 clinical audiograms
23%
Hearing loss (dB HL)
normal range
Tone frequency (kHz)
B
Baseline
Day 1
Day 3
Day 5
Day 7+
ABR w1 threshold (dB SPL)
Tone frequency (kHz)
C
DPOAE threshold (dB SPL)
Tone frequency (kHz)
D
GluR2
Ribbon
Stereo cilia
IHC
nerve fibers
Sham
Trauma
IHC synapse survival (%)
Cochlear frequency (kHz)
E
OHCs
OHC survival (%)
Cochlear frequency (kHz)
F
Sham - OHC stereocilia in cochlear base
G
Trauma - OHC stereocilia in cochlear base
H
H2O
8 or 32 kHz tones
Trial type
Response
Outcome
Tone
Catch
Lick
No Lick
Hit
Miss
False alarm
Withold
I
Tone level (dB SPL)
threshold
Trial number
J
Day -1
Day 0
Day 20
Go probability
8 kHz
32 kHz
Catch
Tone level (dB SPL)
K
Behavioral detection threshold (dB SPL)
8k 32k
Trauma
Sham
Day re:exposure

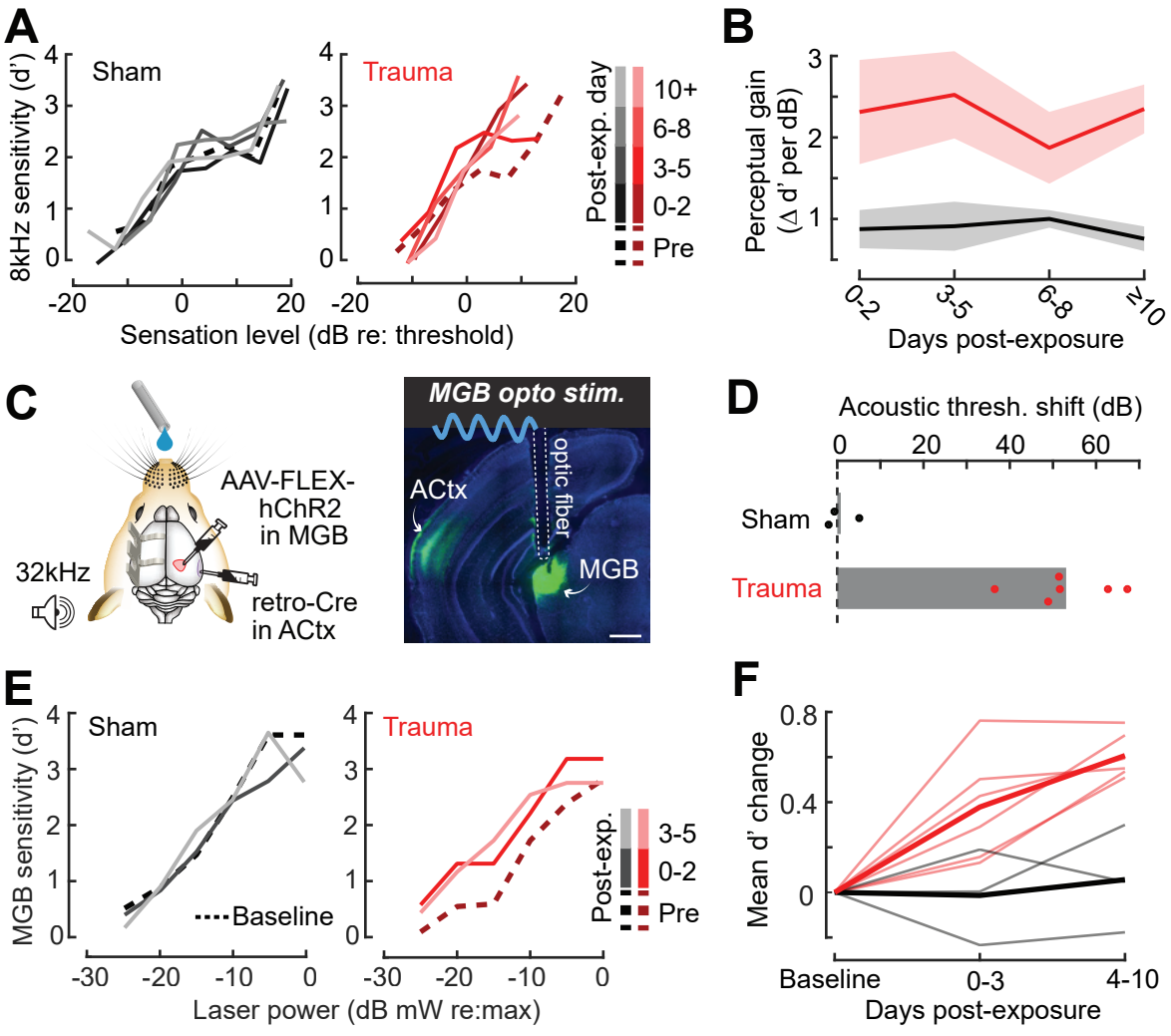
A
Sham
Trauma
8kHz sensitivity (d')
Sensation level (dB re: threshold)
Post-exp. day
10+
6-8
3-5
0-2
Pre
B
Perceptual gain
(Δ d' per dB)
Days post-exposure
0-2
3-5
6-8
≥10
C
AAV-FLEX-
hChR2
in MGB
32kHz
retro-Cre
in ACtx
MGB opto stim.
ACtx
optic fiber
MGB
D
Acoustic thresh. shift (dB)
Sham
Trauma
E
Sham
Trauma
MGB sensitivity (d')
Baseline
Laser power (dB mW re:max)
Post-exp.
3-5
0-2
Pre
F
Mean d' change
Baseline
0-3
4-10
Days post-exposure

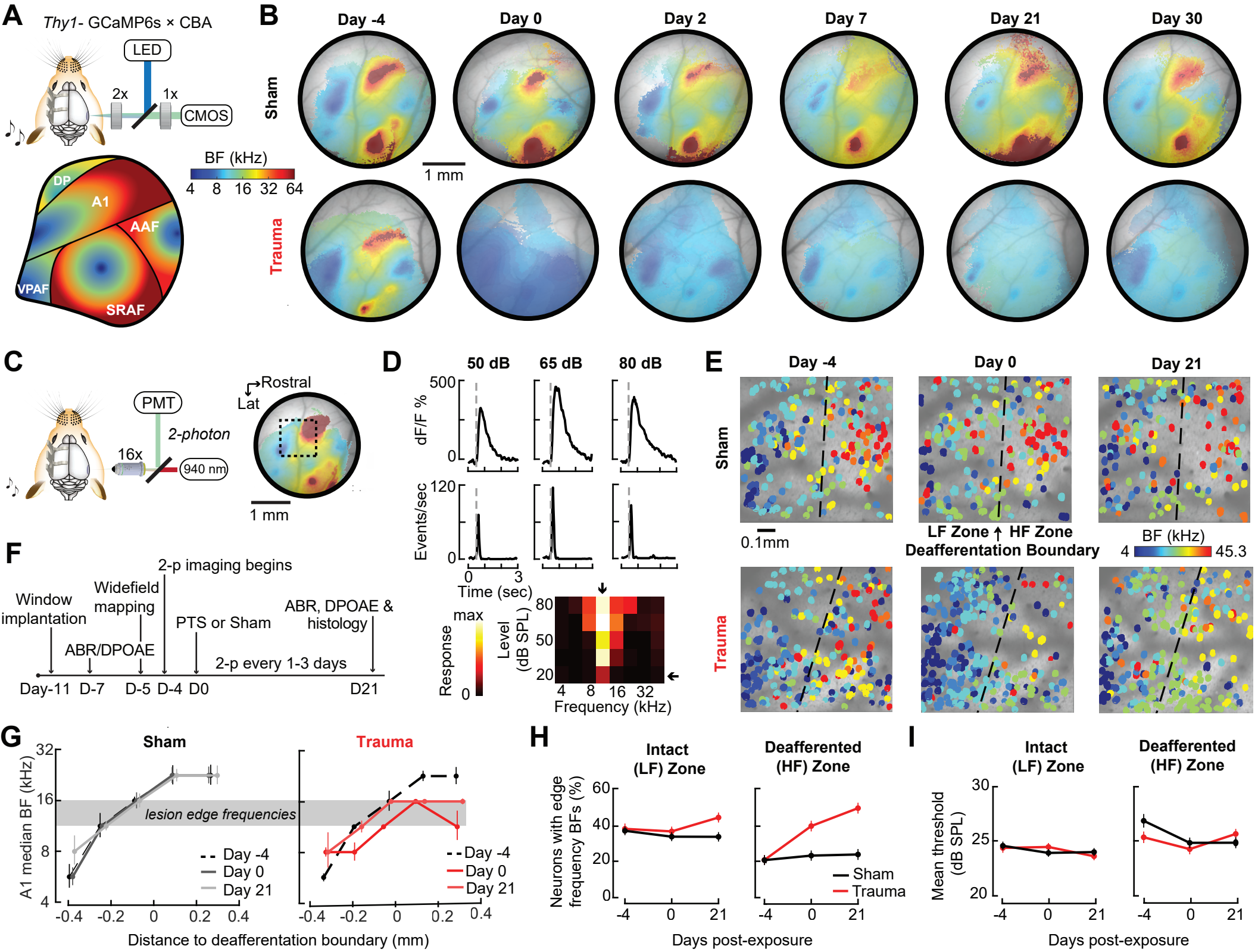
A
Thy1- GCaMP6s × CBA
LED
2x
1x
CMOS
BF (kHz)
4 8 16 32 64
DP
A1
AAF
VPAF
SRAF
B
Day -4
Day 0
Day 2
Day 7
Day 21
Day 30
Sham
Trauma
1 mm
C
PMT
2-photon
16x
940 nm
Rostral
Lat
1 mm
D
50 dB
65 dB
80 dB
dF/F %
500
0
Events/sec
120
0
0 3
Time (sec)
max
Response
0
Level (dB SPL)
80
50
20
4 8 16 32
Frequency (kHz)
E
Day -4
Day 0
Day 21
Sham
Trauma
0.1mm
LF Zone ↑ HF Zone
Deafferentation Boundary
BF (kHz)
4 45.3
F
2-p imaging begins
Window implantation
Widefield mapping
PTS or Sham
ABR, DPOAE & histology
ABR/DPOAE
2-p every 1-3 days
Day-11 D-7 D-5 D-4 D0 D21
G
Sham
Trauma
A1 median BF (kHz)
32
16
8
4
lesion edge frequencies
Day -4
Day 0
Day 21
-0.4 -0.2 0 0.2 0.4
Distance to deafferentation boundary (mm)
H
Intact (LF) Zone
Deafferented (HF) Zone
Neurons with edge frequency BFs (%)
60
40
20
0
-4 0 21
Sham
Trauma
Days post-exposure
I
Intact (LF) Zone
Deafferented (HF) Zone
Mean threshold (dB SPL)
30
25
20
-4 0 21
Days post-exposure

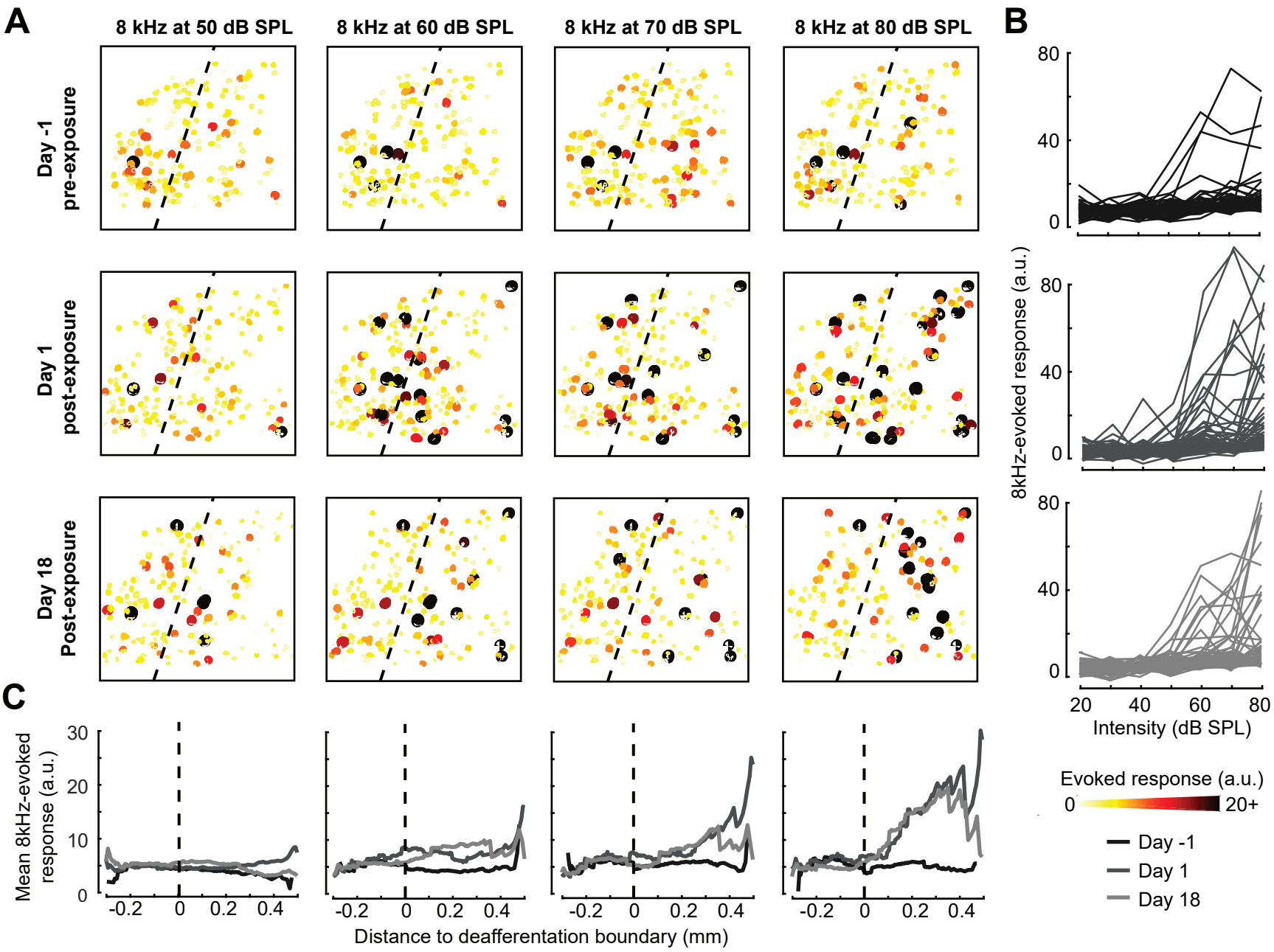
A
8 kHz at 50 dB SPL
8 kHz at 60 dB SPL
8 kHz at 70 dB SPL
8 kHz at 80 dB SPL
Day -1
pre-exposure
Day 1
post-exposure
Day 18
Post-exposure
B
8kHz-evoked response (a.u.)
Intensity (dB SPL)
Evoked response (a.u.)
0
20+
Day -1
Day 1
Day 18
C
Mean 8kHz-evoked response (a.u.)
Distance to deafferentation boundary (mm)

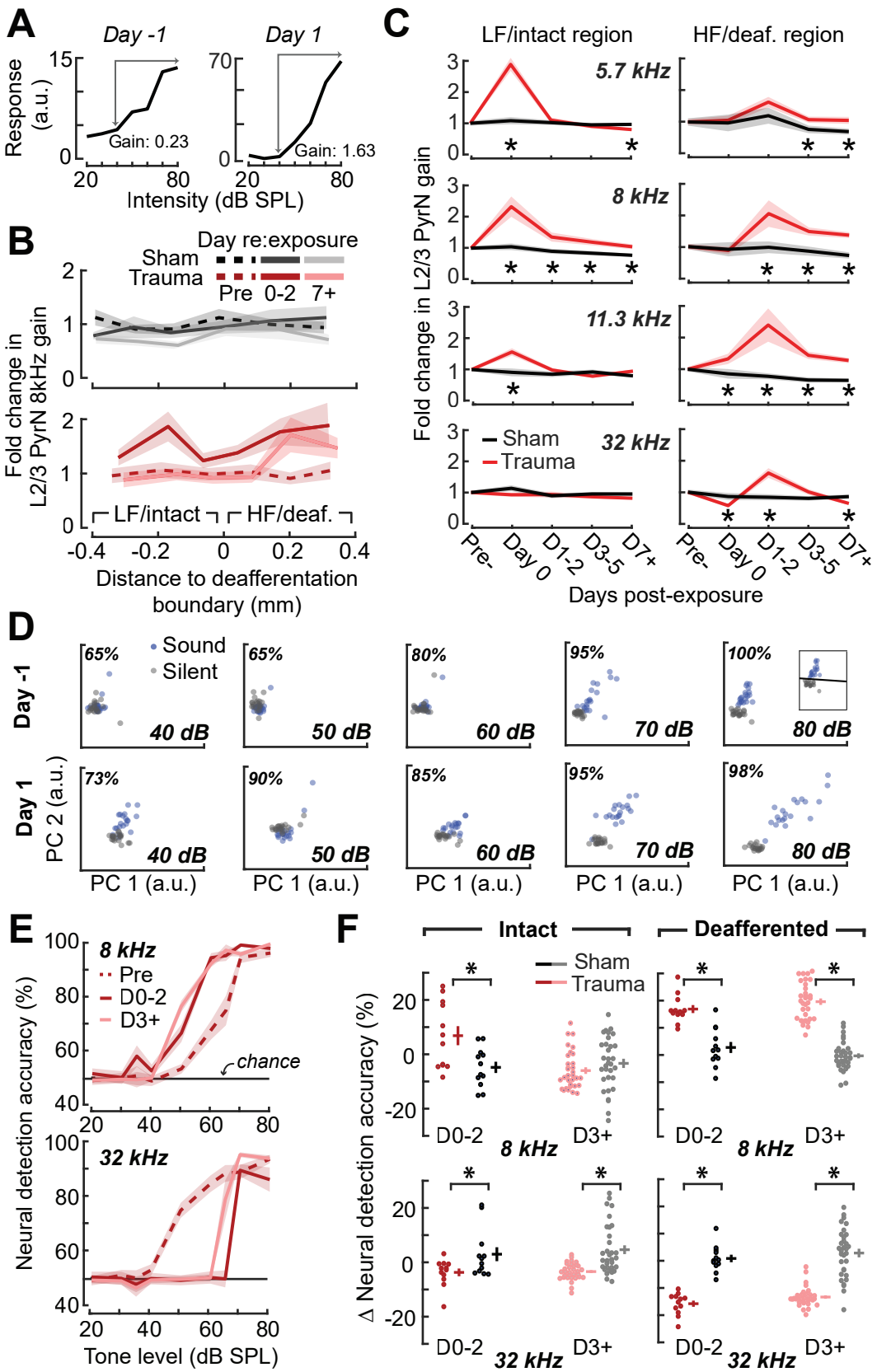
A
Day -1
Day 1
Response (a.u.)
Gain: 0.23
Gain: 1.63
Intensity (dB SPL)
B
Day re:exposure
Sham
Trauma
Pre 0-2 7+
Fold change in L2/3 PyrN 8kHz gain
LF/intact
HF/deaf.
Distance to deafferentation boundary (mm)
C
LF/intact region
HF/deaf. region
5.7 kHz
8 kHz
11.3 kHz
32 kHz
Fold change in L2/3 PyrN gain
Pre-
Day 0
D1-2
D3-5
D7+
Days post-exposure
D
Sound
Silent
Day -1
Day 1
PC 2 (a.u.)
PC 1 (a.u.)
E
8 kHz
Pre
D0-2
D3+
chance
32 kHz
Neural detection accuracy (%)
Tone level (dB SPL)
F
Intact
Deafferented
Sham
Trauma
Δ Neural detection accuracy (%)
D0-2
D3+
8 kHz
32 kHz

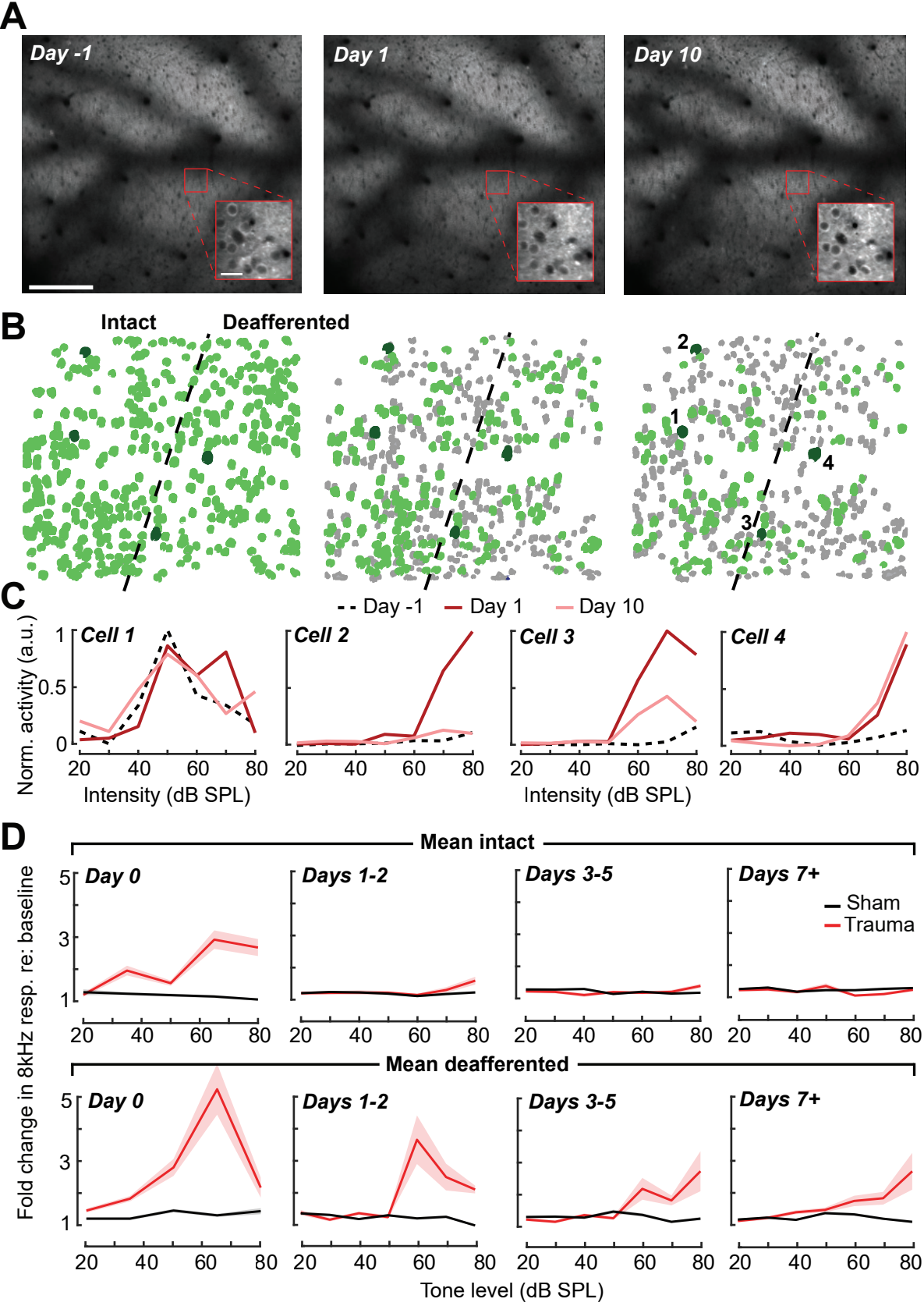
A
Day -1
Day 1
Day 10
B
Intact
Deafferented
1
2
3
4
C
Day -1
Day 1
Day 10
Cell 1
Cell 2
Cell 3
Cell 4
Norm. activity (a.u.)
Intensity (dB SPL)
Intensity (dB SPL)
D
Mean intact
Day 0
Days 1-2
Days 3-5
Days 7+
Sham
Trauma
Mean deafferented
Fold change in 8kHz resp. re: baseline
Tone level (dB SPL)

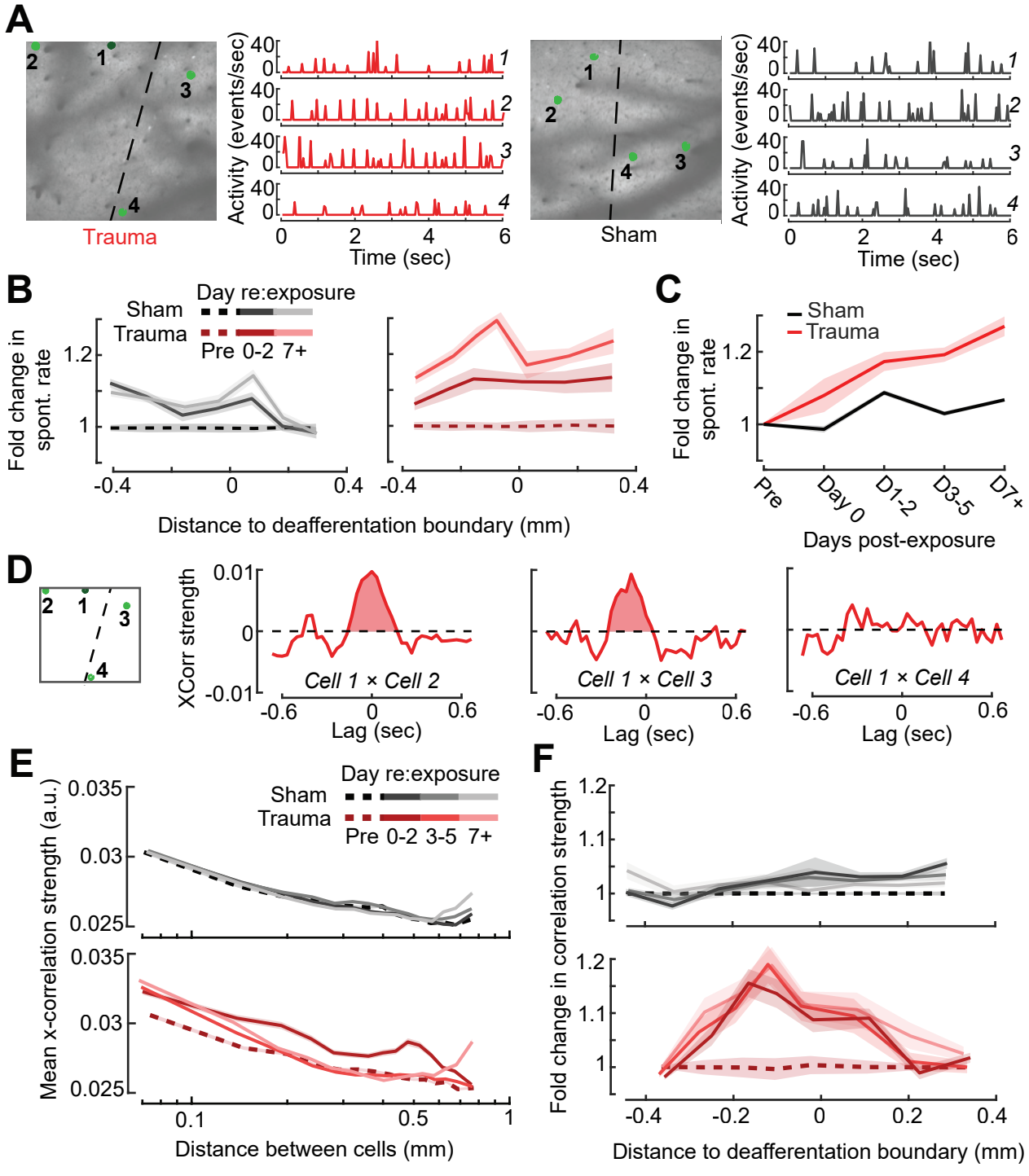
A
Trauma
Activity (events/sec)
Time (sec)
Sham
B
Day re:exposure
Sham
Trauma
Pre 0-2 7+
Fold change in spont. rate
Distance to deafferentation boundary (mm)
C
Sham
Trauma
Fold change in spont. rate
Pre
Day 0
D1-2
D3-5
D7+
Days post-exposure
D
XCorr strength
Cell 1 × Cell 2
Cell 1 × Cell 3
Cell 1 × Cell 4
Lag (sec)
E
Day re:exposure
Sham
Trauma
Pre 0-2 3-5 7+
Mean x-correlation strength (a.u.)
Distance between cells (mm)
F
Fold change in correlation strength
Distance to deafferentation boundary (mm)

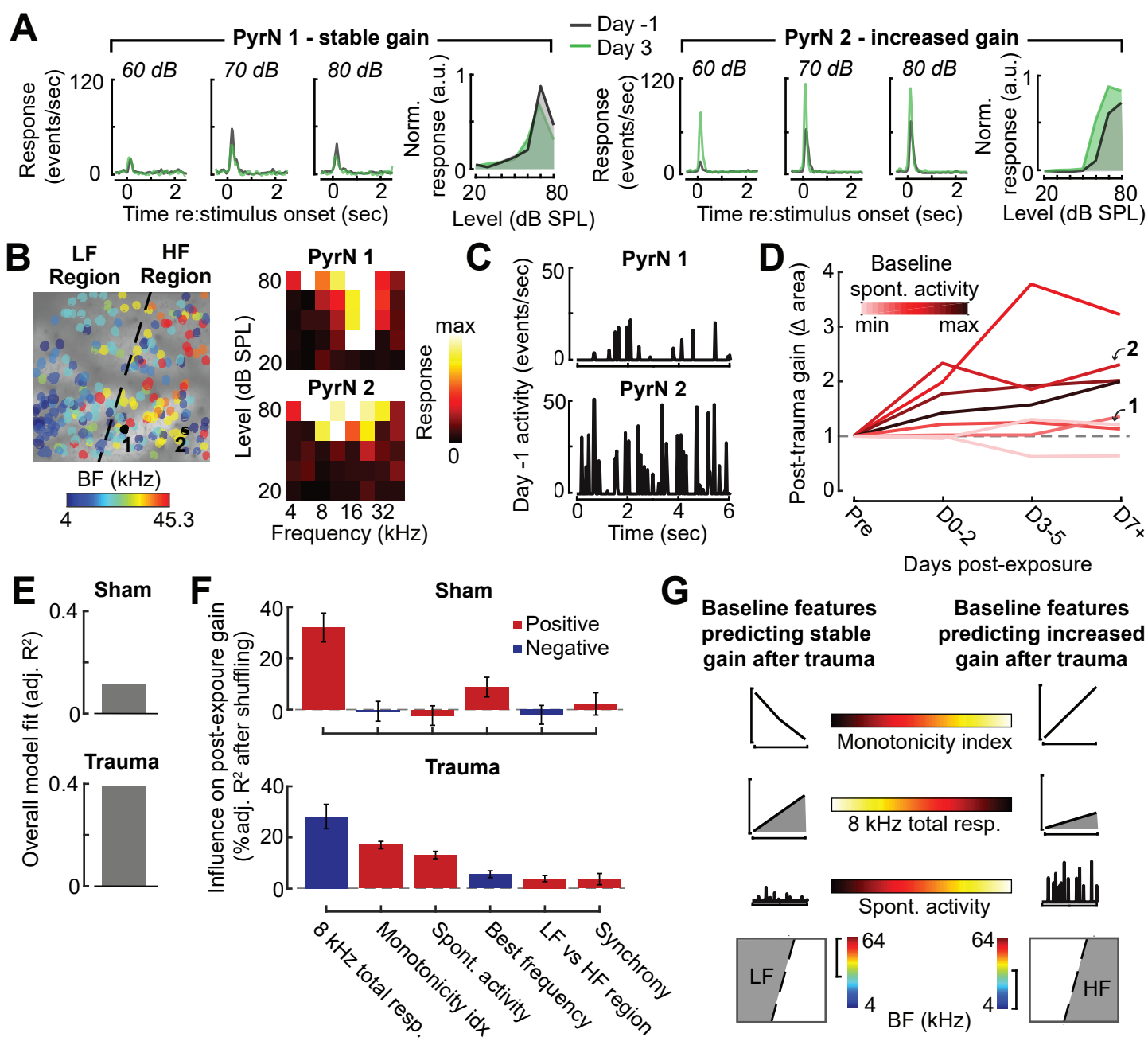
A
PyrN 1 - stable gain
PyrN 2 - increased gain
Day -1
Day 3
60 dB
70 dB
80 dB
Response (events/sec)
Time re:stimulus onset (sec)
Norm. response (a.u.)
Level (dB SPL)
B
LF Region
HF Region
BF (kHz)
4
45.3
PyrN 1
PyrN 2
Level (dB SPL)
Frequency (kHz)
Response
max
C
PyrN 1
PyrN 2
Day -1 activity (events/sec)
Time (sec)
D
Baseline spont. activity
min
max
Post-trauma gain (Δ area)
Pre
D0-2
D3-5
D7+
Days post-exposure
E
Sham
Trauma
Overall model fit (adj. R²)
F
Sham
Trauma
Positive
Negative
Influence on post-exposure gain (% adj. R² after shuffling)
8 kHz total resp.
Monotonicity idx
Spont. activity
Best frequency
LF vs HF region
Synchrony
G
Baseline features predicting stable gain after trauma
Baseline features predicting increased gain after trauma
Monotonicity index
8 kHz total resp.
Spont. activity
LF
HF
BF (kHz)

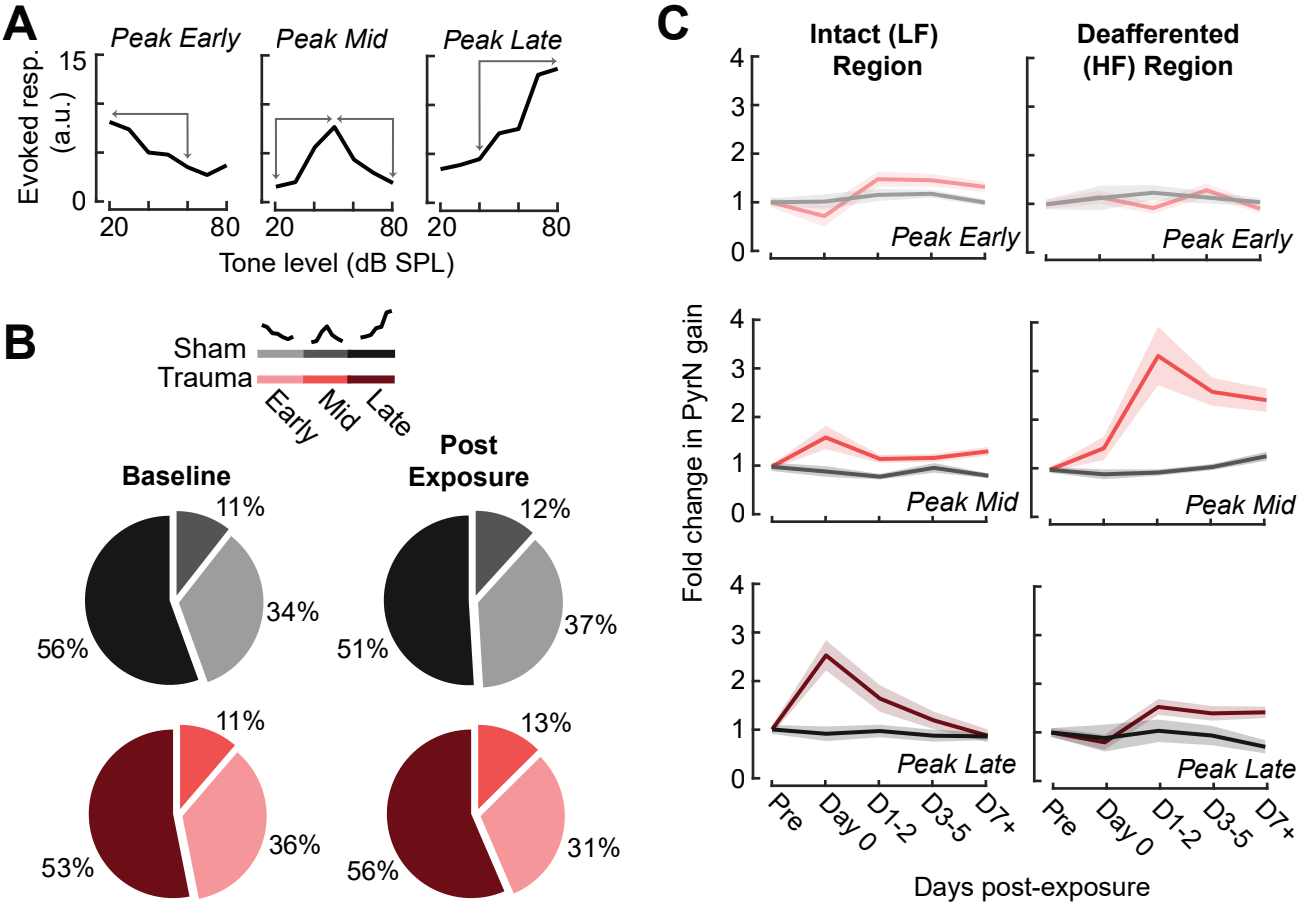
A
Peak Early
Peak Mid
Peak Late
Evoked resp. (a.u.)
15
0
20
80
Tone level (dB SPL)
B
Sham
Trauma
Early
Mid
Late
Baseline
Post Exposure
11%
34%
56%
12%
37%
51%
11%
36%
53%
13%
31%
56%
C
Intact (LF) Region
Deafferented (HF) Region
Peak Early
Peak Mid
Peak Late
Fold change in PyrN gain
Pre
Day 0
D1-2
D3-5
D7+
Days post-exposure

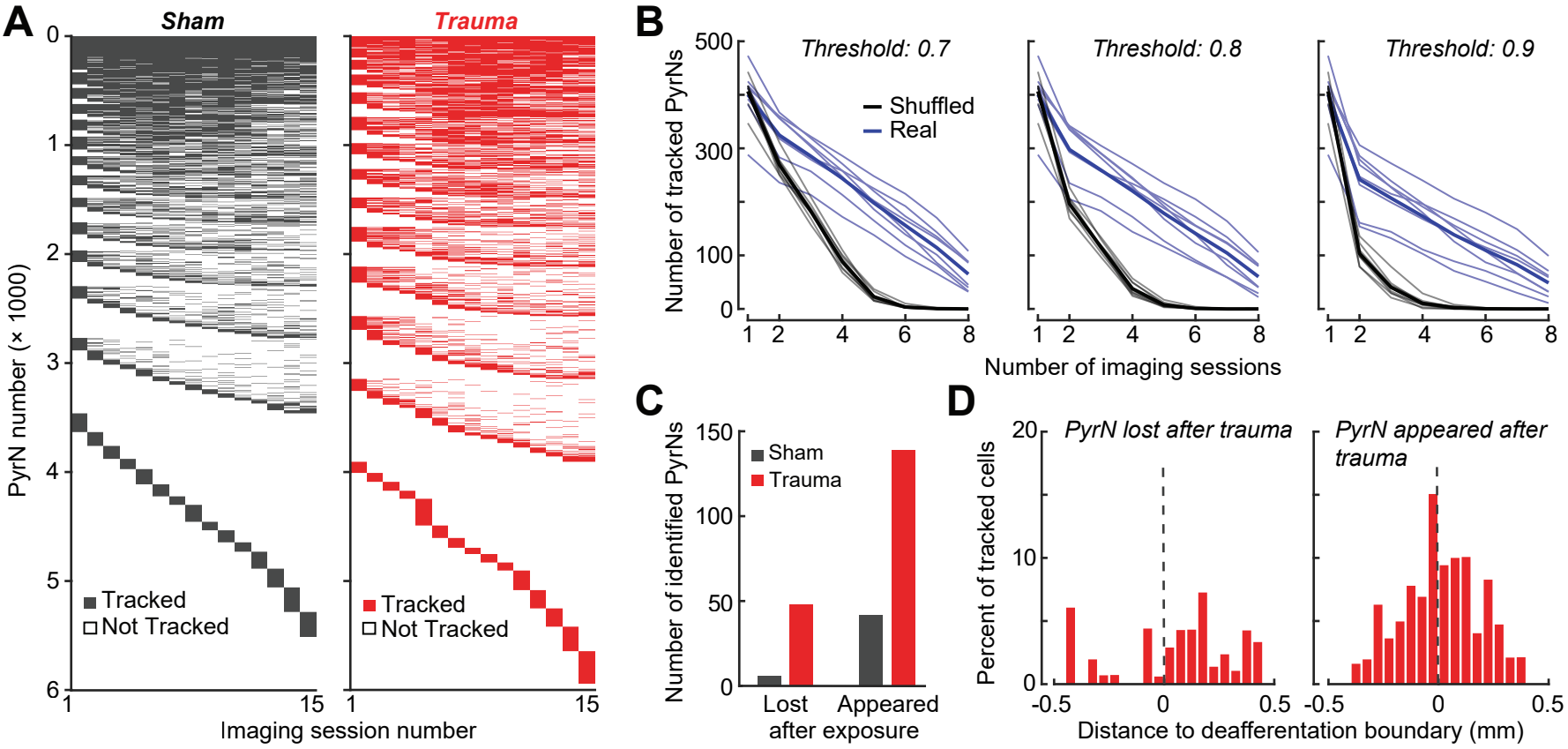
A
Sham
Trauma
PyrN number (× 1000)
0
1
2
3
4
5
6
Tracked
Not Tracked
Tracked
Not Tracked
1
15
1
15
Imaging session number
B
Threshold: 0.7
Threshold: 0.8
Threshold: 0.9
Shuffled
Real
Number of tracked PyrNs
500
300
100
0
1 2 4 6 8
Number of imaging sessions
C
Number of identified PyrNs
150
100
50
0
Sham
Trauma
Lost
Appeared
after exposure
D
PyrN lost after trauma
PyrN appeared after trauma
Percent of tracked cells
20
10
0
-0.5
0
0.5
Distance to deafferentation boundary (mm)

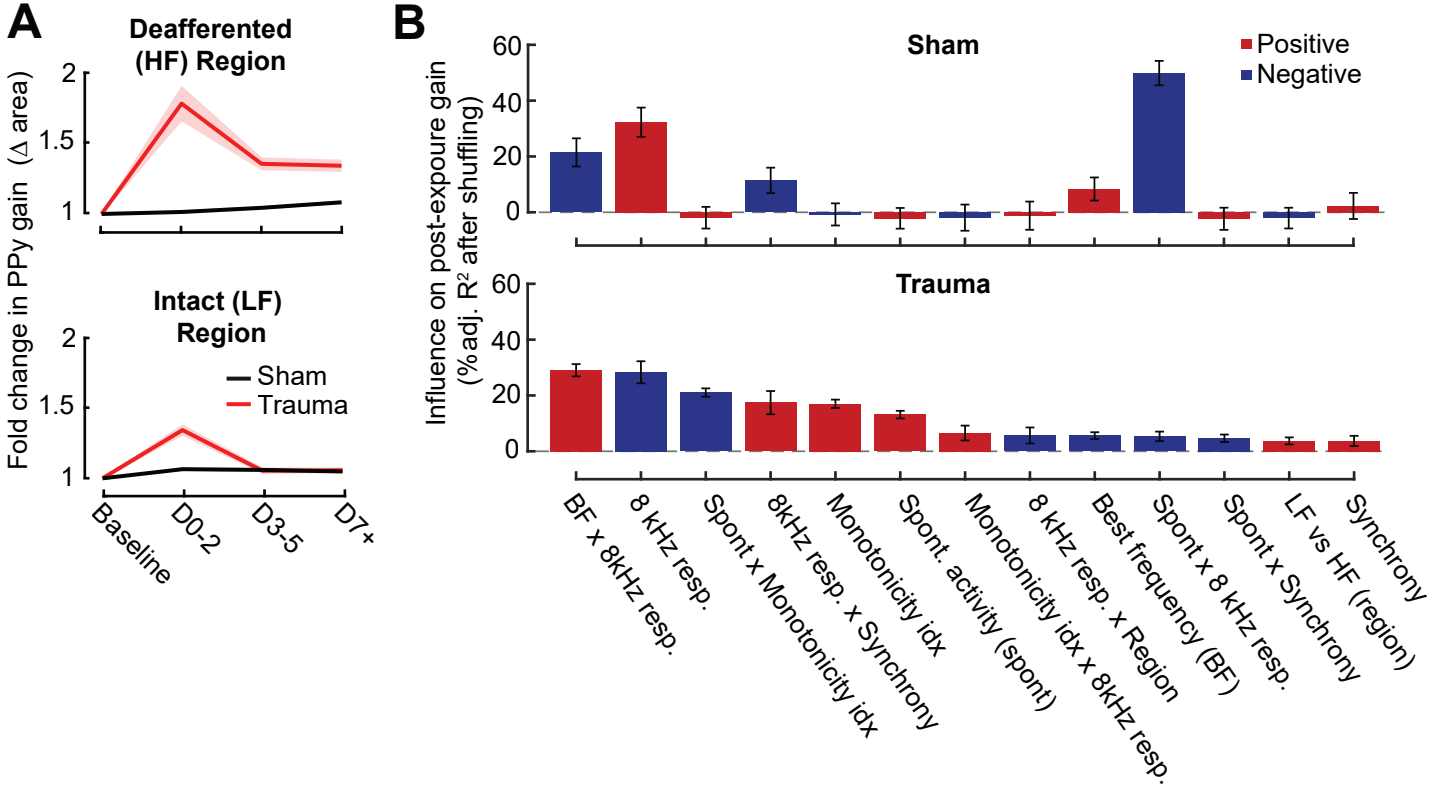
A
Deafferented
(HF) Region
Fold change in PPy gain (Δ area)
2
1.5
1
Intact (LF)
Region
Sham
Trauma
Baseline
D0-2
D3-5
D7+
B
Sham
Positive
Negative
Trauma
Influence on post-exposure gain
(% adj. R² after shuffling)
60
40
20
0
BF x 8kHz resp.
8 kHz resp.
Spont x Monotonicity idx
8kHz resp. x Synchrony
Monotonicity idx
Spont. activity (spont)
Monotonicity idx x 8kHz resp.
8 kHz resp. x Region
Best frequency (BF)
Spont x 8 kHz resp.
Spont x Synchrony
LF vs HF (region)
Synchrony